Oceanic subduction to continental collision in the NE Proto-Tethys revealed by Early Paleozoic eclogites with high-T granulite facies overprinting in the East Kunlun orogenic belt, northern Tibet

Wenxiao Zhou[1*], Feng Chang[2], Bo Huang[3,4], Bin Xia[5*], Dong Fu[4,6], Ernest Chi Fru[7], Haiquan Li[1], Xinbiao Lü[8], Cheng Mao[8]

[1]*Institute of Geological Survey, China University of Geosciences, Wuhan 430074, China*

[2]*School of Earth and Space Sciences, Peking University, Beijing 100871, China*

[3]*Badong National Research and Observation Station for Geohazards, China University of Geosciences, Wuhan 430074, China*

[4]*Central for Global Tectonics, School of Earth Sciences, China University of Geosciences, Wuhan 430074, China*

[5]*School of Earth Sciences, China University of Geosciences, Wuhan 430074, China*

[6]*State Key Laboratory of Geological Processes and Mineral Resources, China University of Geosciences, Wuhan 430074, China*

[7] *School of Earth and Environmental Sciences, Centre for Geobiology and Geochemistry, Cardiff University, Cardiff CF10 3AT, Wales, the United Kingdom*

[8] *School of Earth Resources, China University of Geosciences, Wuhan 430074, China*

* Corresponding authors: zhouwenxiao@cug.edu.cn (W.X. Zhou); xiabin@cug.edu.cn (B. Xia)

ABSTRACT

The East Kunlun orogenic belt (EKOB) in the northern Tibetan Plateau records a long-term accretionary and collisional history in the northeastern Proto-Tethys Ocean, important for reconstructing the paleogeography of Early Paleozoic East Asia. Here we present an integrated petrology, geochemistry, geochronology, and metamorphic *P–T* study of newly found eclogites in the middle Nuomuhong segment of the EKOB. The eclogites are composed mainly of garnet, omphacite and low sodium clinopyroxene, amphibole and plagioclase with minor orthopyroxene, biotite, quartz, accessory rutile, ilmenite, titanite and zircon. Detailed petrographic observations, conventional geothermobarometry and phase equilibrium modeling, point to the presence of five metamorphic mineral assemblages with corresponding *P–T* conditions related to: (1) prograde M_1 stage *P–T* estimates >14.0 kbar/~470–506 °C; (2) P_{max} M_2 eclogite facies stage *P–T* conditions of ~26 kbar/~570°C; (3) early retrograde M_3 high-*P* granulite facies stage; (4) subsequent M_4 retrograde medium-*P* granulite facies at T_{max} of ~860–900°C; and (5) later M_5 retrograde amphibolite facies stage *P–T* conditions of <6.2 kbar/~710–730°C. These *P–T* estimates define a clockwise *P–T* path characterized by heating during the P_{max} formation of the eclogite facies, to the T_{max} exhumation stage for the granulite lithologies, the latter of which is identified for the first time in retrograde eclogites from the EKOB. Whole-rock geochemical composition indicate a mid-oceanic ridge basalt (MORB) affinity for the eclogites protoliths and a fragmented oceanic crust origin. SHRIMP zircon U–Pb isotopic analyses for the eclogite yielded two groups of weighted mean $^{206}U/^{238}Pb$ ages of 464±8 Ma and 419±4 Ma, interpreted as the ages of the eclogite protolith and the lower threshold for peak eclogite facies metamorphism, respectively. Our new data, together with regional eclogite facies metamorphism, suggest a ca. 520–460 Ma age for the subduction of

the eastern Kunlun oceaic crust, within the northern Proto-Tethys Ocean, to a depth of ~83 km, with early subduction–accretionary orogenesis occurring at ca. 419 Ma. Overprinting by high-*T* granulite facies, linked to the maturation of the collisional orogenesis, point to exhumation of the middle to shallow oceanic crust at this time. Collectively, the preserved eclogite and high-temperature (*T*) granulite mineral assemblage provide new constraints on the tectonic evolution and detailed accretionary-to-collisional orogenesis of the Proto-Tethys Ocean. They suggest that the ca. 428–411 Ma subduction-collisional event marked the termination of the Proto-Tethys Ocean and the eventual formation of a ~500-km-long, high to ultra-high pressure metamorphic belt in the EKOB.

Keywords: eclogite; subduction; continental collision; Proto-Tethys Ocean; East Kunlun; northern Tibet

INTRODUCTION

Eclogite is a dense high pressure (HP) to ultra-high pressure (UHP) metamorphic rock comprised dominantly of omphacite and garnet, commonly associated with suture zones of accretionary and collisional orogenic belts (Bingen et al., 2001; Dobretsov, 1991; Hertgen et al., 2016; Klonowska et al., 2016; Meng et al., 2016; Sajeev et al., 2013; Schorn and Diener, 2017; Smith, 1984; Sobolev et al., 1986). Some eclogites may undergo high temperature (HT) and even ultra-high temperature (UHT) metamorphic overprinting during collisional orogenesis (Wang et al., 2022a; Wang et al., 2021). The reconstruction of the pressure–temperature–time (*P*–*T*–*t*) path for eclogite, reliant on proper estimates of pressure–temperature (*P*–*T*) evolution and determination of precise metamorphic ages, is thus important for deciphering the thermal history and large-scale tecto-orogenic processes along paleo-subduction-collision interfaces (Hertgen et al., 2016; Wang et al., 2017).

The Tethyan orogenic system, comprised of the Proto-Tethys, Paleo-Tethys to the Neo-Tethys, is the largest collisional orogen on Earth (Dong et al., 2018; Şengör, 1984; Zhao et al., 2018). Its reconstruction represents one of the most important and yet difficult to resolve puzzles in solid earth science research. In northern Tibet, northwest China, two early Paleozoic HP/UHP metamorphic belts exist (Fig. 1). The succession includes a HP metamorphic belt in the North Qilian orogenic belt and a UHP metamorphic belt in the northern Qaidam block, with interpreted formation in oceanic and continental subduction zone environments, respectively, during the evolution of the Proto-Tethyan orogenic belts (Han et al., 2015; Song et al., 2018a; Song et al., 2014; Song et al., 2012; Song et al., 2007; Yu et al., 2013a; Zhang et al., 2010a; Zhang et al., 2016; Zhang et al., 2015a; Zhang et al., 2008; Zhang et al., 2009; Zhang et al., 2015b). Recently, a several-kilometer-

78 wide HP/UHP metamorphic belt was recognized along the Central East Kunlun Fault in the East
79 Kunlun orogenic belt (EKOB, Fig. 1) (Chen et al., 2016; Meng et al., 2015a; Qi et al., 2014; Qi et
80 al., 2016a; Song et al., 2018b). This metamorphic belt was regarded as a subduction-collision suture
81 zone that records the tectonic evolution of the eastern Kunlun Ocean-a branch in the Proto-Tethys
82 Ocean (Bi et al., 2022; Song et al., 2018b). despite decades of igneous and metamorphic research,
83 the tectonic affinity of eclogite protoliths, the mechanism for subduction and exhumation, the
84 details of orogenesis in the EKOB and the evolution of the Proto-Tethys Ocean remain controversial
85 (Dong et al., 2018; Feng et al., 2023; Sun et al., 2022; Wang et al., 2022b; Yu et al., 2020a). Some
86 researchers suggested that the late Ordovician Tumuleke glaucophane schist and associated gabbro
87 ($^{40}Ar/^{39}Ar$ age: 445 ± 2 Ma) may signify the termination of oceanic subduction and the beginning of
88 continental collision in late Ordovician (Mo et al., 2007), whereas others proposed that the final
89 closure of the ocean basin occurred in mid-Silurian (Lu et al., 2010). New data suggest two
90 discontinuous and distinct orogenic cycles from the Proto-Tethys to the Paleo-Tethys in the EKOB
91 (Feng et al., 2023).

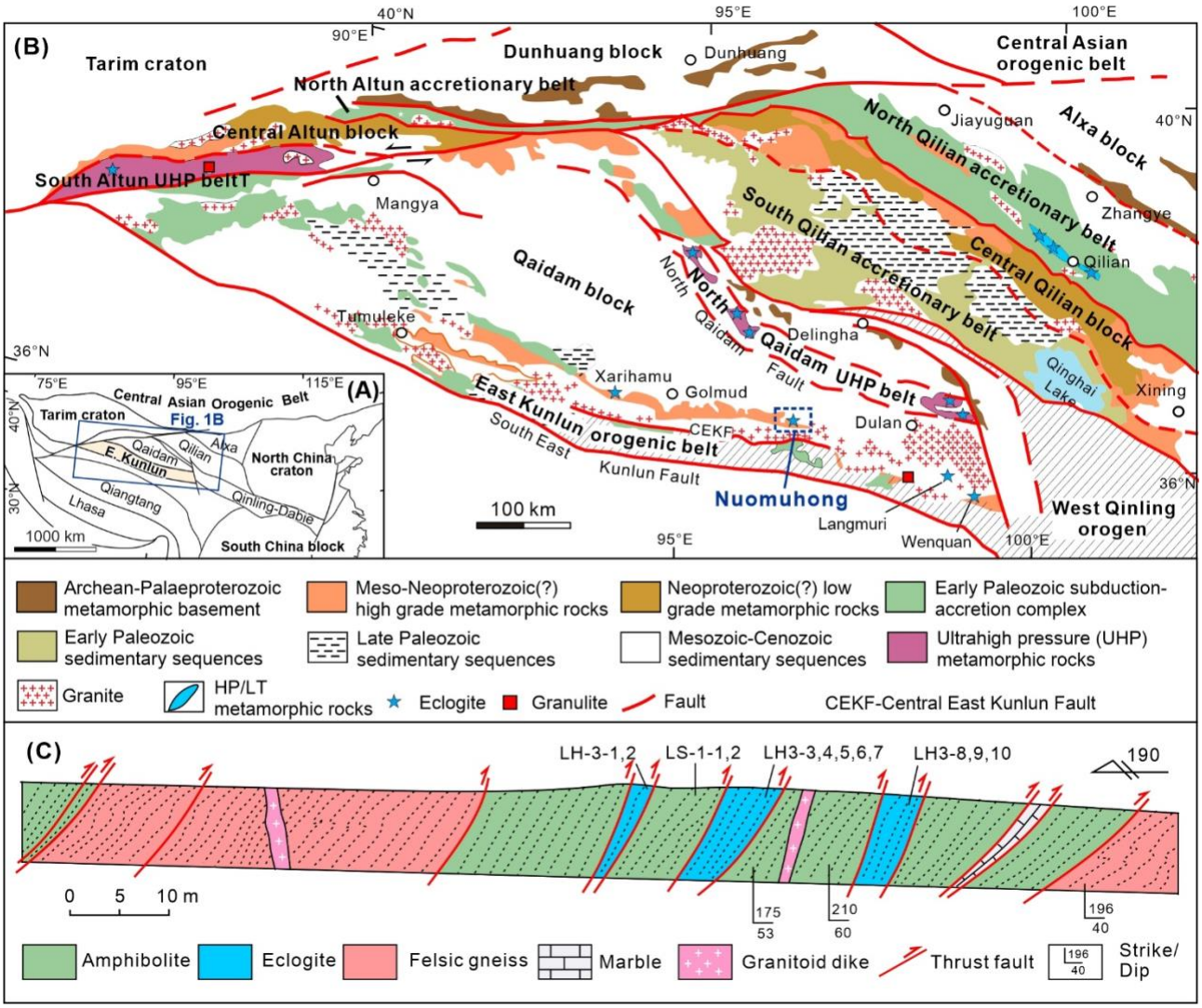

Figure 1. (A) Tectonic sketch map showing the major cratons and orogenic belts in northern China (Fu et al., 2022a) . (B) Simplified geological map showing tectonic units in the northern Tibet Plateau (modified after (Meng et al., 2017; Zhang et al., 2015b; Zhang et al., 2017)). The locations of eclogites in the Nuomuhong area and other segments of the EQOB are marked (Meng et al., 2013b; Qi et al., 2014; Qi et al., 2016a; Song et al., 2018b). (C) An approximately N-S structural cross-section of the Nuomuhong area showing the main rock types and the location of samples.

In this contribution, we report a newly found eclogite that was overprinted by high-*T* granulite facies metamorphism in the Nuomuhong region in the middle segment of the EKOB (Figs. 1B and

1C). We present an integrated study combining petrology, whole-rock geochemistry, and SHRIMP zircon U–Pb ages from the eclogite to constrain its protolith and metamorphic *P–T–t* evolution, linked to two-stage ocean crust subduction and continental collision in the northeastern Proto-Tethys domain. The new metamorphic evidence together with regional geological data in the EKOB, highlight the early Paleozoic accretionary history and collisional orogenesis of the Proto-Tethyan EKOB.

GEOLOGICAL SETTING AND SAMPLING

The East Kunlun orogenic belt (EKOB) in the northern Tibet Plateau is bounded by the Qaidam block in the north, the Qiangtang-Songpan terrane in the south, and the West Kunlun orogenic belt separated by the Altyn Tagh strike-slip fault in the northwest (Li et al., 2018a; Meng et al., 2017; Song et al., 2018b; Wang et al., 2022b; Zhang et al., 2012; Zhang et al., 2015b) (Figs. 1A and 1B). The EKOB is subdivided into three tectonic belts. These include the North and South Kunlun belts, and the Muz Tagh-Anemaqen and Hoh Xil-Bayan Har Terranes by the North Kunlun Fault (NKLF), Middle Kunlun Fault (MKLF), South Kunlun Fault (SKLF), Muz Tagh-Anemaqen Fault (MAF), from north to south (Jiang et al., 1992; Luo et al., 1999; Meng et al., 2013b; Yang et al., 1986; Yu et al., 2020b).

The North Kunlun belt is composed of Precambrian metamorphic rocks, late Paleozoic volcanic-sedimentary rocks, and Paleozoic and Triassic granitoids. The Precambrian rocks are dominated by gneisses, migmatite and amphibolite of the Paleoproterozoic Jinshuikou Group (Jiang et al., 1992) and the greenschist facies carbonate and clastic rocks of the Mesoproterozoic Binggou Group (Meng et al., 2018). Zircon U–Pb ages of the gneiss and amphibolite from the Jinshuikou

Group suggest that high-grade metamorphism at ca. 1.8 Ga was followed by a two-phase tecto-thermal event at ca. 1.0–0.9 Ga and ca. 400 Ma (Chen et al., 2008a; He et al., 2016; Meng et al., 2013a; Song et al., 2018b; Zhou et al., 2020). Zircon ages of the schists from the Xiaomiao Group point to the deposition of metasedimentary rocks during the Mesoproterozoic and subsequent metamorphism at ca. 400 Ma (He et al., 2016; Wang et al., 2003a). These basement rocks were later overlain by late Paleozoic volcanic-sedimentary rocks. Three phases of magmatism events, which include the Neoproterozoic gneissic granites deposited at ca. 1006–870 Ma (Chen et al., 2015; Meng et al., 2013b). The ca. 466–390 Ma Paleozoic diorites and granites and the ca. 250–200 Ma Triassic granites, formed in this belt (Dong et al., 2018).

The South Kunlun belt (SKT) is mainly composed of Paleozoic–Triassic sedimentary and volcanic rocks, with some Precambrian facies and Early Paleozoic and Permain–Triassic granites. It stretches from the Wenquan area in the east, through the Wanbaogou area in the middle, to Chader Tagh in the west. This succession witnessed the Caledonian to Indosinian events, including the Wanbaogou island arc and the Qingshuiquan back arc basin activities. Although the Qingshuiquan ophiolites and the volcanic rocks of the Wanbaogou Formation are the key indicators, their formation age and genetic settings have been disputed (Chen et al., 2011; He et al., 2016; Liu et al., 2016; Xu et al., 2016; Yu et al., 2020b).

The Central East Kunlun arc-accretionary complex belt is represented by the 540–460 Ma Early Paleozoic ophiolite, the 550–390 Ma arc volcanic and sedimentary rocks, widely regarded as a subduction-collision suture zone (Dong et al., 2018; Li et al., 2018b; Meng et al., 2015b; Yang et al., 2004; Zhou et al., 2020). Eclogite facies rocks are sporadically distributed in the Xiarihamu in the west, and Kehete and Wenquan areas in the east, forming a >500 km HP–UHP metamorphic belt

(Meng et al., 2013b; Qi et al., 2014; Qi et al., 2016b). Recently, coesite-bearing UHP metamorphic rocks were discovered in the Kehete area in the eastern segment (Fig. 1B)(Bi et al., 2018; Bi et al., 2020).

Eclogites were newly found at the Nuomuhong valley approximately 150 km SE from Golmud city in the central segment of the HP–UHP metamorphic belt in East Kunlun (Fig. 1B). Lithologies at Nuomuhong are comprised mainly of granitic gneiss, eclogite, and amphibolite with minor marble composition (Figs. 1C and 2). Eclogite occurs as lenses or blocks of 5–15 meters in diameter enclosed in the host gneiss of the Paleoproterozoic Jinshuikou Group (Figs. 1C and 2A, C). The eclogite has mainly been retrogressed (Fig. 2B, F) and at places, amphibolite can be found at the outer edge of the eclogite block (Fig. 2B). The Amphibolite occurs as massive or foliated structures, with some intercalated marble lenses/slices (Fig. 2D). In a ~500-meter-long cross-section from east to west along the Nuomuhong valley, dozens of eclogite and/or retrograde eclogite were sampled from three eclogite blocks (Figs. 1C and 2D). Three samples (LH3–2, LH3–4 and LH3–5) were selected for detailed petrographic observations and mineral chemistry analyses. In addition, the eclogite sample LH3–4 was performed for phase equilibrium modeling and SHRIMP U–Pb dating. The host felsic gneiss shows a granoblastic texture and consists of mainly plagioclase, potassium feldspar, quartz and biotite, with minor garnet (Fig. 2C–E). Twelve samples including 10 retrograde eclogites and 2 garnet amphibolites were selected for whole-rock major and trace element analyses. Mineral abbreviations are after Whitney and Evans (2010).

165

166 **Figure 2.** Field photographs of eclogite at Nuomuhong, in East Kunlun. (A) Eclogite block enclosed in the
167 host felsic gneiss. (B) Eclogite retrograded to amphibolite at edges. The red dashed line marks the boundary
168 between the retrograde eclogite and amphibolite. (C) The red dashed line showing the boundary between
169 retrograde eclogite and the host felsic gneiss. (D) Marble intercalated in amphibolite that shows a foliated
170 structure. (E) The host felsic gneiss consisted mainly of felsic minerals, biotite and garnet. (F) The retrograde
171 eclogite consisted of mainly garnet, clinopyroxene, amphibole and quartz.

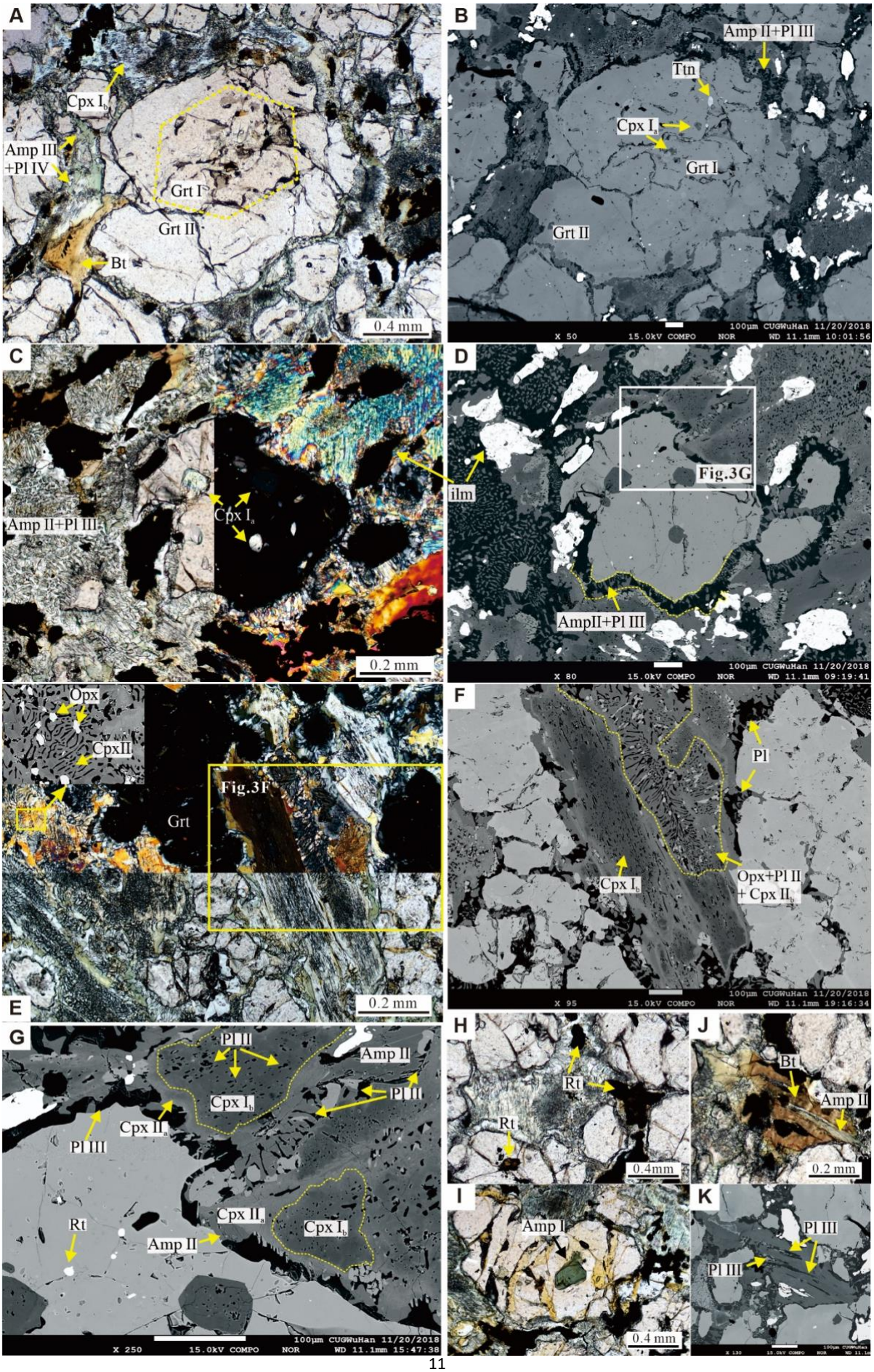
A
Cpx I$_b$
Amp III
+Pl IV
Grt I
Grt II
Bt
0.4 mm
B
Amp II+Pl III
Ttn
Cpx I$_a$
Grt I
Grt II
X 50 15.0kV COMPO NOR WD 11.1mm 10:01:56
C
Amp II+Pl III
Cpx I$_a$
0.2 mm
D
ilm
Fig.3G
AmpII+Pl III
X 80 15.0kV COMPO NOR WD 11.1mm 09:19:41
E
Opx
CpxII
Grt
Fig.3F
0.2 mm
F
Pl
Cpx I$_b$
Opx+Pl II
+ Cpx II$_b$
X 95 15.0kV COMPO NOR WD 11.1mm 19:16:34
G
Pl III
Amp II
Cpx I$_b$
Pl II
Cpx II$_a$
Pl III
Rt
Cpx II$_a$
Cpx I$_b$
Amp II
X 250 15.0kV COMPO NOR WD 11.1mm 15:47:38
H
Rt
Rt
0.4mm
J
Bt
Amp II
0.2 mm
I
Amp I
0.4 mm
K
Pl III
Pl III

Figure 3. Photomicrographs of representative eclogites at Nuomuhong, EKOB. (A) A large garnet porphyroblast from the eclogite LH3–5 showing apparent zoning with abundant inclusions in the reddish core and minor in the light rim. Amphibole (Amp II), plagioclase, ilmenite and biotite (Bt) developed around the garnet. (B) Backscattered electron image (BSE) of the garnet porphyroblast in panel A showing inclusions of titanite (Ttn) and omphacite (Cpx I_a) in the core. (C–D) Corona of plagioclase (Pl III) + amphibole (Amp II) ± ilmenite (LH3–4) around a relict garnet porphyroblast with inclusions of omphacite (Cpx I_a). Symplectite of plagioclase (III) + amphibole develops in the matrix; (E–F) Symplectite of orthopyroxene (Opx)+ plagioclase (Pl II) around relict omphacite in matrix from the sample LH3–4. Corona of symplectite amp II + Pl develops around relict garnet and low-sodic clinopyroxene (Cpx II_a; light-colored in BSE) develops around relict omphacite porphyroblast (Cpx I_b; dark-colored in BSE). (G) Locally enlarged BSE image in panel D showing transition from relict omphacite porphyroblast (Cpx I_b; with no Opx) to clinopyroxene porphyroblast (Cpx II_b; with Opx), then to symplectite of Amp II + Pl II; (with Opx). Corona of plagioclase (Pl III) + amphibole (Amp II) rims garnet; (H) Rutile inclusions in garnet or in matrix from the sample LH3–2, showing partial replaced by ilmenite; (I) Amphibole (Amp I) included in garnet from sample LH3–2. (G–K) Plane-polarized photo with corresponding BSE image showing Biotite around amphibole (Amp II) from sample LH3–5.

PETROLOGY

Petrography and Mineral Compositions

Representative minerals were analyzed using a JEOL JXA–8230 electron probe micro-analyzer (EPMA) in China University of Geosciences (Wuhan). The detailed analytical method and results listed in Supplementary Text and Table S1-S6, respectively. The Nuomuhong EKOB eclogites are

generally characterized by a massive structure with porphyroblastic/granoblastic texture. They comprise mainly 30–40 vol.% garnet, 25–30 % clinopyroxene, 15–20 % amphibole, 10–15 % plagioclase and 2–5 % biotite, with minor 2–5 % orthopyroxene and 1–3 % quartz, and accessory rutile/ilmenite, apatite, titanite and zircon (Fig. 3).

Garnet

Euhedral to subhedral 0.2–2.0 mm grain size crystals typically characterize the porphyroblastic garnet minerals in representative sample LH3-2, LH3-4 and LH3-5. The garnet crystals typically contain a greater amount of omphacite, rutile/ilmenite/titanite, epidote + plagioclase, amphibole and quartz inclusions in the reddish core, compared to the light-colored rim (Fig. 3A, B; Fig. 4C). These observations are consistent with an apparent core-rim structure revealed by back-scatted electronic (BSE) photos (Fig. 3A, B; Fig. 4B). The garnet minerals commonly show an embayed texture and tend to be replaced by amphibole, plagioclase and an ilmenite corona (Fig. 3A-D, G). In places, aggregated epidote minerals and albite develop as inclusions in the garnet (Fig. 4C).

A chemical profile for one large garnet porphyroblast in the eclogite sample LH3-4 shows clear compositional zonation for almandine, pyrope, grossular and spessartine (Fig. 4D, E). From core to rim, X_{Alm} [= $Fe^{2+}/(Fe^{2+} + Mg + Ca + Mn)$] increases from 0.55 to 0.61, and then decreases to 0.52; X_{Grs} [= $Ca/(Fe^{2+} + Mg + Ca + Mn)$] decreases slightly from 0.32 to 0.28, before a sharp increase to 0.34 and then decreases again to 0.28; X_{Prp} [= $Mg/(Fe^{2+} + Mg + Ca + Mn)$] increases from 0.05 to 0.18; and X_{Sps} [= $Mn/(Fe^{2+} + Mg + Ca + Mn)$] decreases from 0.09 to <0.01. The X_{Sps} profile shows a classic bell-shaped zoning pattern, interpreted to represent growth zonation.

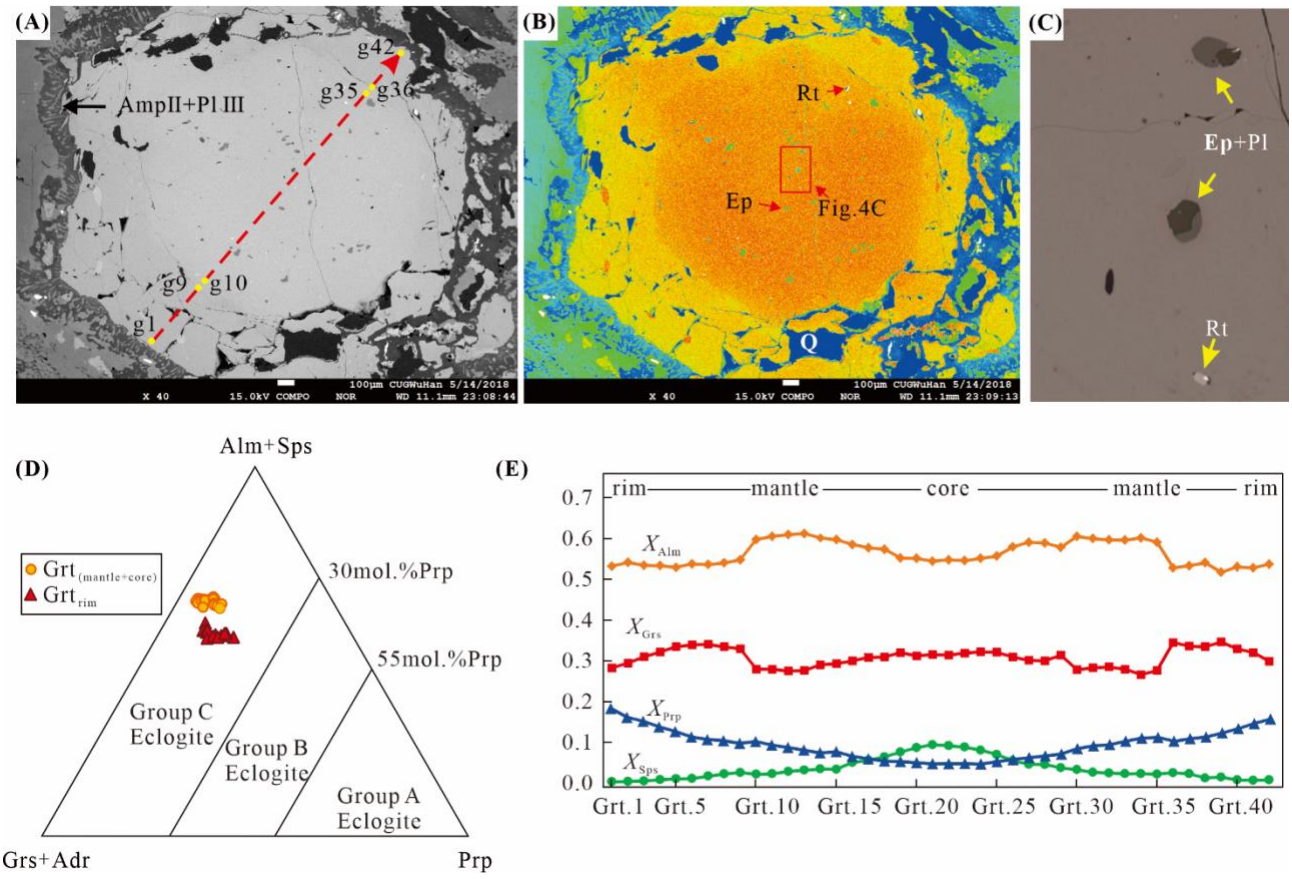

Figure 4. (A–B) BSE photographs of a large porphyroblastic garnet (LH3-4). The red dashed line represents cross section analysis by EPMA. (C) Enlarged photo in panel B with aggregated inclusions of Ep + Pl. (D) Diagram showing compositional variations of garnet. Both $Grt_{(mantle+core)}$ (Grt I) and Grt_{rim} (Grt II) are suggested to belong to group C-type according to Coleman et al. (1965). (E) Zoning profile of X_{Alm}, X_{Sps}, X_{Prp} and X_{Grs} across garnet in the eclogite samples LH3-4 from Nuomuhong.

Clinopyroxene

Based on variations of occurrences and mineral compositions, clinopyroxene in sample LH3–4 show the following 4 archetypal subdivisions: (1) Cpx I, omphacite present as Cpx I_a, inclusions in garnet (Figs. 3C-D) or as Cpx I_b matrix rock-forming minerals (Figs. 3A and 3C–3E). Most of Cpx I_b phases are partially replaced by low-sodium clinopyroxene and plagioclase-containing symplectite. Cpx I_a generally has higher Jd content than Cpx I_b (Fig. 5A); (2) Cpx II occurs as Cpx

229 II_a together with plagioclase-constituting symplectite Cpx I_b rims, or as Cpx II_b together with
230 orthopyroxene and plagioclase replacing Cpx II_a. The Cpx II_a phases generally possess a higher Jd
231 composition with lower MgO and FeO contents than Cpx II_b (Table S2-S3, Fig. 5B). Both Cpx II_a
232 and Cpx II_b have lower SiO_2 and Jd component, but higher MgO and FeO concentration than Cpx I
233 (Table S2-S3, Fig. 5B). Away from Cpx I, Cpx II presents a lighter color in BSE images (Figs. 3E
234 and 3F), showing increasing Wo enrichment (Fig. 5B).

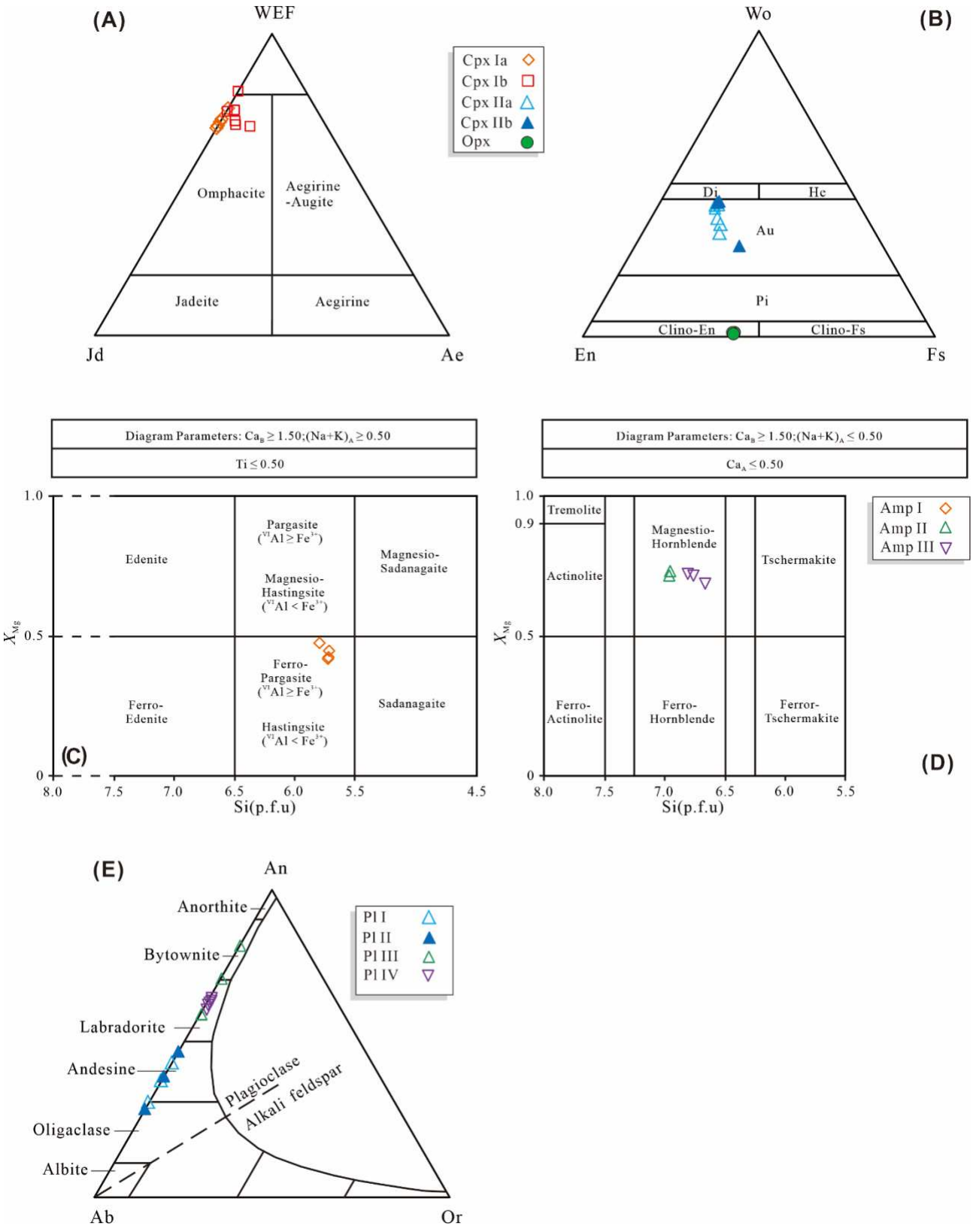

Figure 5. Mineral chemistry diagrams. (A–B) Ternary classification diagrams for clinopyroxene from the Nuomuhong eclogites, after Morimoto (1988); (A) Classification diagram for Quad–Jd–Ae; (B) Classification diagram for Wo–En–Fs. (C–D) Classification diagrams for amphiboles for the Nuomuhong

eclogite, after Leake et al. (2004) and Song et al. (2018b). (E) Ab–An–Or diagram showing the composition of plagioclase, after Smith (1974); Ab=X_{Na}=Na/(Ca + K + Na); An=X_{Ca}=Ca/(Ca + K + Na); Or =X_K=K/(Ca + K + Na).

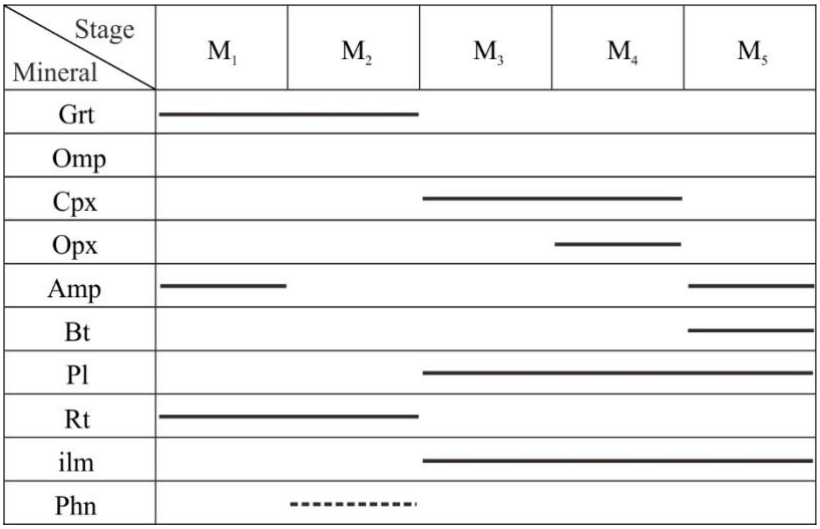

Figure 6. Sequences of mineral assemblages for different metamorphic stages. Solid lines indicate minerals present in the samples, whereas the dashed line refers to inferred minerals.

Amphibole

Amphibole in sample LH3–4 occurs as inclusions (Fig. 3I) in garnet (Amp I), or together with plagioclase as corona (Fig. 3C–3E) around garnet (Amp II), or as rock-forming minerals in matrix (Amp III, Figs. 3A and 3B). Amp I exhibits a lower Si content of 5.71–5.72 (p.f.u.) with a higher ^{IV}Al composition of 2.22–2.29 (p.f.u.). Its $Mg^{\#}$ [= (Mg/(Mg+Fe^{2+})] of 0.42–0.45 and $(Na+K)_A \leq$ 0.50 (p.f.u.), corresponds to ferro-pargasite (Fig. 5C) according to Leake et al. (1997). Compared to Amp I, a higher Si content of 6.95–6.96 (p.f.u.) and lower ^{IV}Al content of 1.04–1.05 (p.f.u.), characterizes Amp II. Both Amp II and Amp III have similar $Mg^{\#}$ of 0.69–0.72 and $(Na+K)_A \leq 0.50$ (p.f.u.), indicative of a magnestio-hornblende composition (Table S4, Fig. 5D).

Plagioclase

Plagioclase occurs either as inclusions in garnet (Fig. 4C), or together with matrix amphibole, clinopyroxene and/or orthopyroxene (Fig. 3D, G). When included in garnet, plagioclase (LH3-2, Pl I) co-exists with epidote, constituting composite inclusions and is albite (Fig. 4C). Matrix plagioclase (LH3–4, Pl II) either forms symplectite after omphacite (Fig. 3E, F, G), or occurs together with Amp II in the corona surrounding garnet (LH3–5, Pl III) (Fig. 3D, G). In places, large LH3–2 Pl IV plagioclase shows texture equilibration with Amp III amphibole (Fig. 3A).On the other hand, $An_{28\text{-}47}Ab_{53\text{-}72}$ Pl II plagioclase has an oligoclase-andesine affinity, whereas the $An_{61\text{-}64}Ab_{36\text{-}39}$ Pl III and $An_{60\text{-}82}Ab_{18\text{-}40}$ Pl IV forms, characterized by higher An values, are related to labradorite (Fig. 5E, Table S5).

Orthopyroxene

Fine-grained matrix Opx (LH3–2) develops mainly in association with Pl II and Cpx II_b-containing symplectite after Cpx II_a (Fig. 3E–3G). In the Wo-En-Fs diagram, Opx is shown to belong to hypersthene with X_{En} of 56.3–56.9 and X_{Fs} of 41.8–42.4 (Table S6, Fig. 5B).

Minor minerals

The occurrence of minor fine-grained biotite in the matrix (LH3–4) and around garnet (Fig. 3A) or amphibole (Fig. 3J), is interpreted to represent the formation of phengite during early metamorphism (Fig. 6). Epidote and anorthosite exist as composite inclusions in garnet but absent in the matrix (Fig. 4C). Rutile, partially replaced by ilmenite/titanite, is present both as inclusions in garnet and in the matrix (Figs. 3H and 4C).

Minerology and metamorphic stages

Based on petrographic observations and mineral compositions, the following five mineral assemblages can be inferred for the eclogite at Nuomuhong, east Kunlun: (1) M_1 prograde metamorphic stage amphibole eclogite facies evidenced by Cpx I_a + Amp I + Rt + Ep + Qz inclusions in garnet core and mantle/garnet core-mantle compositions; (2) Metamorphic M_2 peak stage eclogite facies evidenced by Grt rim, matrix rock-forming Cpx I_b, Rt and quartz. Omphacite inclusions in zircons from Group #2 (Fig. 7) are further inferred to belong to metamorphic peak stage mineral assemblage; (3) Early retrograde metamorphic stage high-pressure granulite facies (M_3), is substantiated by Cpx II_a with low Jd symplectite content and plagioclase (Pl II) rimming Cpx I_b; (4) Subsequent retrograde metamorphic stage medium-pressure granulite facies (M_4) represented by garnet surrounding Opx coronas and Opx + Pl II + Cpx II_b replacing Cpx II_a symplectite; 5) Later retrograde metamorphic stage amphibolite facies (M_5) indicated by Amp II and Pl II garnet-surrounding intergrowth and large-grained matrix Pl IV and Amp III. In addition, Ilm replacing Rt and the occurrence of matrix Bt (replacing phengite), likely formed at this stage (Fig. 6).

METAMORPHIC *P–T* CONDITIONS

In this study, to reconstruct the metamorphic *P–T* path for eclogite formation at Nuomuhong, we selected representative eclogite LH3–4 samples for further study based on the progressive growth zonation retained in porphyroblastic garnet and the relatively complete mineral sequences recorded in these samples. We use both conventional geothermobarometry and phase equilibrium

300 modelling to constrain *P–T* conditions for different metamorphic stages.

301

302 **Conventional Geothermobarometry**

303 Conventional geothermobarometry, including the garnet–clinopyroxene (Grt–Cpx)
304 thermometry (Ravna, 2000), the Al-in-hornblende barometry (Schmidt, 1992) combined with the
305 amphibole–plagioclase (Amp–Pl) thermometry (Holland and Blundy, 1994), and the two-pyroxene
306 thermometry (Wood, 1973) were used for *P–T* estimates for different stage mineral assemblages. *P–*
307 *T* conditions for prograde stage (M_1) metamophism calculated using the Grt–Cpx thermometry on
308 garnet-core (Grt I) composition, and omphacite (Cpx I_a), indicate formation at metamorphic
309 pressure >14 kbar and temperature of 470–506 °C. Grt–Cpx thermometry on garnet rim (Grt II) and
310 matrix omphacite (Cpx I_b), suggest peak stage metamorphism (M_2) occurred at a temperature range
311 of 525–585 °C at a pressure of 20 kbar according to previous studies on eclogite from the EKOB
312 (Meng et al., 2015b; Qi et al., 2014; Qi et al., 2016b; Song et al., 2018b). Calculated retrograde
313 stage (M_4) metamorphic temperature of 860–900 °C using the two-pyroxene thermometry and
314 compositions of orthopyroxene (Opx) and low-sodic clinopyroxene (Cpx II_b), assumes a medium
315 pressure of 6 kbar. The *P–T* conditions for late retrograde stage metamorphis (M_5) using Al-in-
316 hornblende barometry, Amp–Pl thermometry and compositions of large matrix amphibole (Amp III)
317 and plagioclase (Pl IV), point to formation at ~6 kbar and 710–730 °C (Fig. 6).

318

319 **Phase Equilibrium Modelling**

320 Phase diagrams were drawn using the updated March 2014 THERMOCALC software version
321 3.40, and the November 2016 updated version of the associated internally consistent

thermodynamic dataset ds62 (Holland and Powell, 2011). The NCKFMASHTO system Na_2O–CaO–K_2O–FeO–MgO–Al_2O_3–SiO_2–H_2O–TiO_2–O chemical composition was selected for analysis, with *a–x* relationships implemented as follows: amphibole and clinopyroxene (Green et al., 2016); garnet, phengitic muscovite and biotite (White et al., 2014); epidote (Holland and Powell, 2011). Rutile, lawsonite, quartz and H_2O were considered to be in the pure phase. Bulk rock XRF composition was used for modelling after correction of CaO, SiO_2, Al_2O_3 contents for the P_2O_3 and MnO contained in apatite and spessartine. Fe_2O_3 was determined by wet chemistry. The corrected bulk composition in mol% used in phase equilibrium modeling was SiO_2 (51.99), Al_2O_3 (8.51), CaO (11.82), MgO (11.21), FeO (12.26), K_2O (0.11), Na_2O (2.17), TiO_2 (0.92) and O (1.0). H_2O was assumed to be in excess, considering the abundance of various hydrous mineral inclusions (e.g., epidote and amphibole) in garnet.

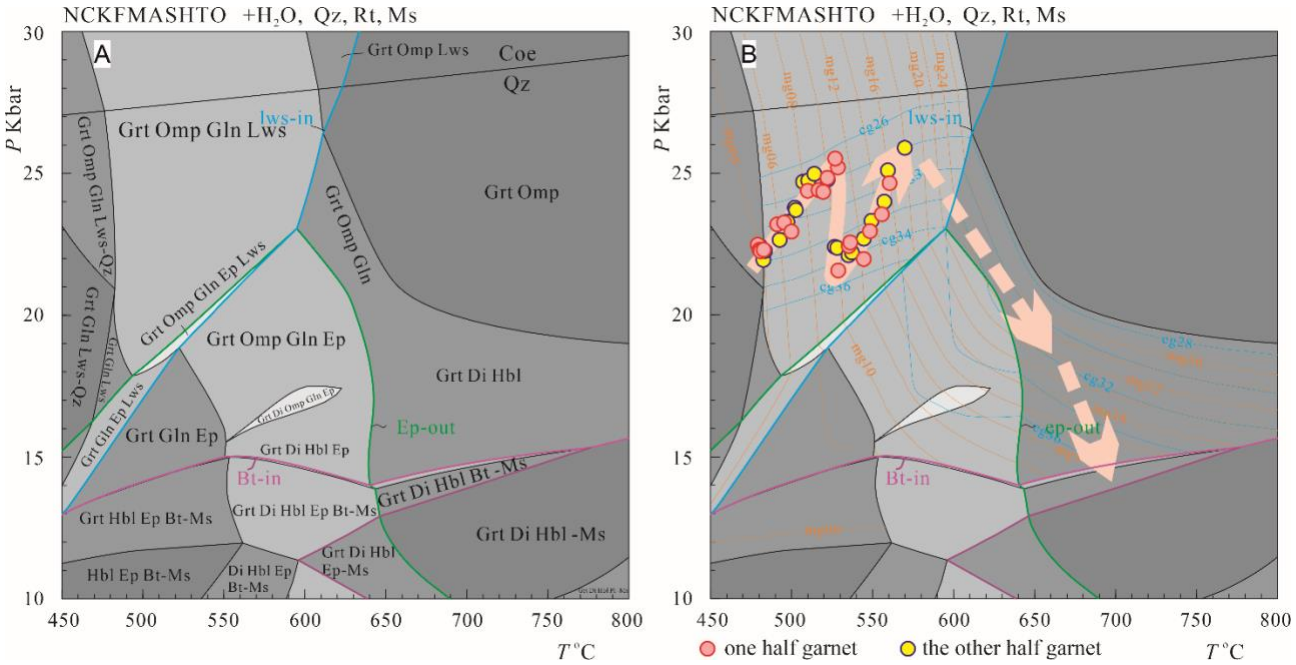

Figure 7. (A) *P–T* pseudosection for eclogite LH3–4 at Nuomuhong in the NCKFMASHTO system. Mineral abbreviations follow Thermocalc dataset (B). cg and mg represent calculated isopleths for grossular [Ca/(Ca+Mg+Fe+Mn)] and pyrope [Mg/(Ca+Mg+Fe+Mn)] endmembers in garnet, respectively. For instance,

337 mg06 denotes 0.06 pyrope and cg26 0.26 grossular. Mineral abbreviations are after Whitney and Evans
338 (2010).

339 The *P–T* pseudosection for the retrograde eclogite LH3–4 had a *P–T* range of 10–30 kbar and
340 450–800 °C (Fig. 7). Figure 8A places the phase assemblage fields of lawsonite at 12–30 kbar and
341 400–600 °C and epidote at 10–23 kbar and 400–635 °C. Lawsonite is replaced by epidote at P <23
342 kbar and T of <595 °C, and by garnet and omphacite at T >595 °C and P >17.5 kbar. In the phase
343 assemblage fields of Grt + Omp (Di) + Gln (Hbl) ± Ep + Qz + Rt + Ms + H_2O, glaucophane
344 gradually changes to hornblende and omphacite to diopside at decreasing pressure. The replacement
345 of muscovite by biotite in the phase assemblage fields occurs at a P range of 14–15.5 kbar before
346 being replaced again by hornblende and clinopyroxene at T >595 °C. Isopleths for 26–36 mol% Grs
347 and 5–26 mol% Prp in garnet have been calculated for the *P–T* range related to the Gln (Hbl)-
348 bearing and Ms-bearing phase assemblage fields (Fig. 7B). In the law-bearing phase assemblage
349 fields, isopleths for Grs in garnet have gentle to moderate positive slopes with Grs values
350 decreasing with pressure, whereas isopleths of Prp in garnet have almost vertical slopes with Prp
351 values increasing with temperature. In the law-absent phase assemblage fields, isopleths for Grs in
352 garnet have vertical to moderate negative slopes with Grs values tending to decrease with rising
353 temperature, whereas the garnet Prp isopleths have moderate negative slopes with Prp values
354 increasing simultaneously with temperature.

355 The observed M_2 peak stage mineral assemblage corresponds to the modelled field with the
356 phase assemblage of Grt + Omp (Di) + Gln (Hbl) + Qtz + Rt + Ms + H_2O at 14.0–26.5 kbar and
357 595–800 °C. However, isopleths for the measured Grs and Prp content in garnet (27–35 mol% and
358 5–18 mol%, respectively) yield *P–T* conditions of 21.5–26 kbar and 480–570 °C in the phase

assemblage field of Grt + Omp + Gln + Lws + Qtz + Rt + Ms + H_2O (Fig. 7B). Both muscovite and lawsonite were not detected in the thin section. The modelled muscovite content in this phase assemblage field was <1.5 mode%. Its low contents may be the reason for non-detection by thin section analysis; or may be pointing to complete retrograde transformation to biotite during the late stage metamorphism as evidenced by the presence of matrix biotite (Fig. 3A, J). Lawsonite may have been present in the peak mineral assemblage but was subsequently replaced by amphibole and clinopyroxene with increasing exhumation *T* and or was replaced by epidote due to effective bulk rock composition in confined equilibration volume (Wei et al., 2010). Aggregates of Ep + Ab (potentially originating from paragonite) as inclusions in garnet may be pseudomorphs produced after lawsonite (Fig. 4C). Both situations correlate with dehydration reactions and may be easily triggered when *T* increases or *P* decreases. The inferred presence of lawsonite during prograde metamorphism has previously been reported in many HP/UHP eclogite terrane based on composite inclusions of Ep/Zo ± Pg/Ab in garnet (Wei et al., 2010; Hamelin et al., 2018). For instance, in western Dabie, epidote inclusions, coupled with paragonite, was interpreted to reflect the former presence of lawsonite (Wei et al., 2010). In this study, because of intense retrogression during post-eclogite facies stages, the eclogite at Nuomuhong has been strongly retrograded with most garnet porphyroblast eplaced by later stage mineral aggregates (e.g., amphibole, plagioclase and ilmenite). However, the well-preserved garnet growth zoning for a carefully selected garnet porphyroblast indicates the prograde information could have been potentially preserved in this refractory mineral. Using phase equilibrium modeling and compositional isopleth geothermobarometry, we interpret the *P–T* regime of 21.5–26 kbar and 480–570 °C for lawsonite stability to represent possible prograde stage *P–T* conditions.

Therefore, the inferred peak mineral assemblage of Grt + Omp + Amp + Qz + Rt at the M_2 stage to correspond to the modelled phase assemblage field of Grt + Omp + Gln + Lws + Qz + Rt + Ms + H_2O at *P* of 21.5–26 kbar and *T* of 480–570 °C. Glaucophane may have been gradually replaced by Na-poor amphibole during decompression. Amphibole inclusion in garnet with higher Na content than that in the matrix, may be assumed as support for this conclusion. Besides, variations of endmembers across the garnet could be indicative of two-stage garnet porphyroblast growth with various *P–T* evolutions, first controlled by increasing pressure and temperature, followed by a second rise in pressure and temperature and then by an eventual decrease in pressure (Fig. 7B). During initial exhumation, lawsonite decomposed and the *P–T* path crossed the modelled phase assemblage of Grt + Omp (Di) + Gln (Hbl) + Qz + Rt + Ms + H_2O with *P–T* conditions of 14.0–26.5 kbar and 595–800 °C. Further exhumation led to the transition of muscovite to biotite and omphacite to diopside and plagioclase, which may correspond to the modelled phase assemblage field of Grt + Di + Hbl + Qz + Rt + Bt + H_2O with *P–T* conditions of 13.0–15.5 kbar and 645–775 °C. However, with a change in the effective bulk rock composition due to the presence of garnet, this *P–T* regime remains uncertain. *P–T* conditions for the formation of orthopyroxene have not been constrained for the change of effective bulk rock composition.

WHOLE-ROCK GEOCHEMISTRY

The analytical procedure for whole rock geochemistry determination is listed in the Supplementary Text, and the results in Supplementary Table S7. The data show that the retrograde eclogites at Nuomuhong are basaltic in composition. They possess low SiO_2 (48.33–51.07 wt.%), high Al_2O_3 (13.39–15.37 %) and CaO contents (10.39–12.75 %), and moderate TiO_2 (1.02–1.32 %)

and Cr (154–290 ppm) compositions. On the AFM [(Na_2O+K_2O) –FeO^T–MgO] diagram, all data fall in the tholeiite series field (Fig. 11E). The retrograded eclogites are relatively low in total rare earth elements abundance (∑REEs=36.31–59.19 ppm). On the chondrite-normalized REE diagram (Fig. 8A), they exhibit nearly flat to enriched REE patterns, without significant Eu anomalies (δEu=0.91–1.05) and are slightly enriched LREE, with La_N/Yb_N ratios of 1.17–2.21. By contrast, the garnet amphibolites exhibit slight LREEs depletion (La_N/Sm_N=0.79–0.90). Primitive mantle-normalized trace element analysis (Fig. 8B), suggests the retrograde eclogites are strongly enriched in Nb and Ta but depleted in Zr and Ti. On the other hand, the garnet amphibolites are enriched with Zr, with Nb–Ta showing significant positive anomalies relative to La.

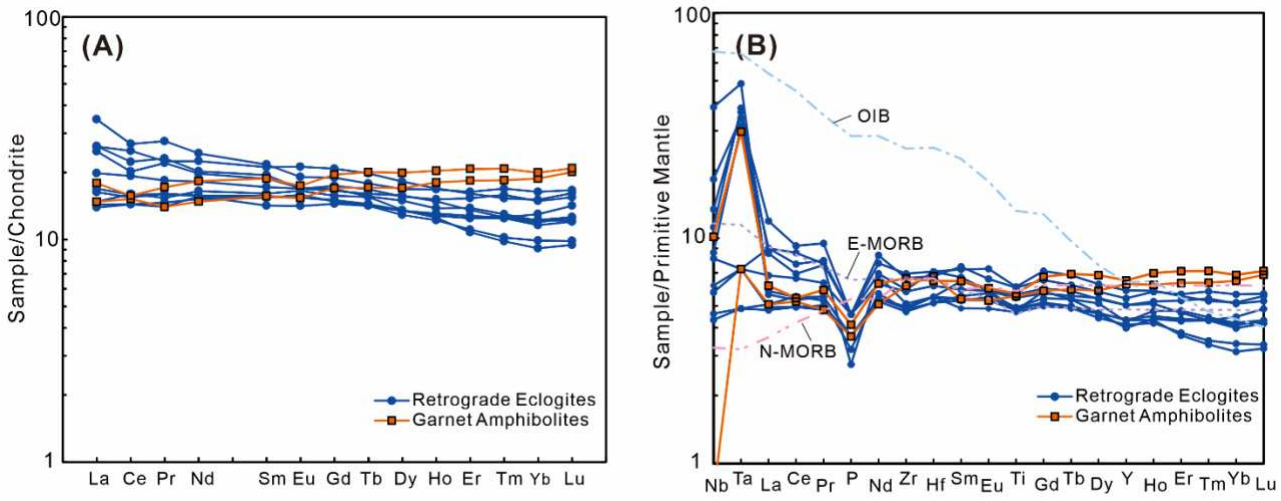

Figure 8. (A) Chondrite-normalized REE distribution patterns. (B) Plots for rimitive mantle-normalized retrograde eclogites and garnet amphibolites. The chondrite and primitive mantle values are from (Sun and McDonough, 1989).

ZIRCON U-Pb DATING

Zircon grains from the LH3–4 eclogite display a euhedral to subhedral morphology, with a tendency to be rounded, being 70–130 μm in length. The majority of the zircons are homogeneous

or show weak or sector zonation in cathodoluminescence (CL) images (Figs. 9A, B), a typical characteristic of a metamorphic origin (Corfu et al., 2003; Wang et al., 2013b; Wu and Zhen, 2004). Some grains have core-rim structures (Fig. 9A), broad zonation and contrast bright cores taken to indicate residual cores that survived metamorphic alteration.

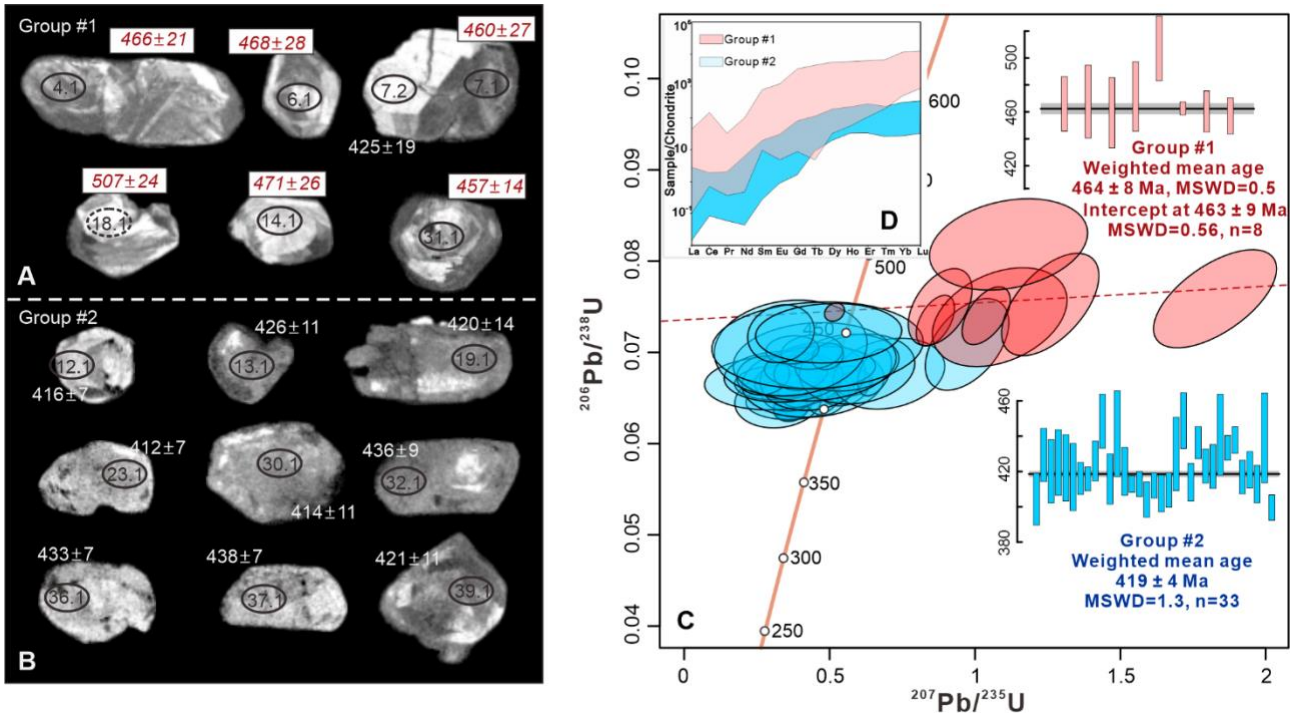

Figure 9. (A–B) Zircon CL images, (C) SHRIMP U–Pb age concordia diagram and weighted mean $^{206}Pb/^{238}U$ ages, and (D) Chondrite-normalized REE distribution patterns for the Nuomuhong retrograde eclogite LH3–4.

A total of 45 analyses were obtained by SHRIMP dating (Table S8). The Th and U contents of most smaples are low, with Th/U ratios <0.1. A majority of the analyses contain near flat heavy REE (HREE) patterns in the chondrite normalized diagram (Fig. 9D). A few of the zircons reveal Th/U ratios >0.1, interpreted as an attribute of the dissolution of Th-enriched minerals such as epidote, under HT conditions (Hermann, 2002; Yu et al., 2013b). The weighted mean of $^{206}Pb/^{238}U$ ages represented two groups, with Group #1 consisting of 8 analyses yielding an intercept age of

463±9 Ma with an MSWD of 0.56 and an identical weighted mean age of 464±8 Ma with an MSWD of 0.5 (Fig. 9C). Group #2, comprised of 33 analyses, yielded a weighted mean age of 419±4 Ma with an MSWD of 1.3 (Fig. 9C). The laser Raman spectroscopy of the inclusions in the second group zircons indicate a omphacite and garnet composition, suggesting that the Group #2 zircons represent a lower age limit for when peak eclogite facies metamorphism occurred (Figs. 10A–10C).

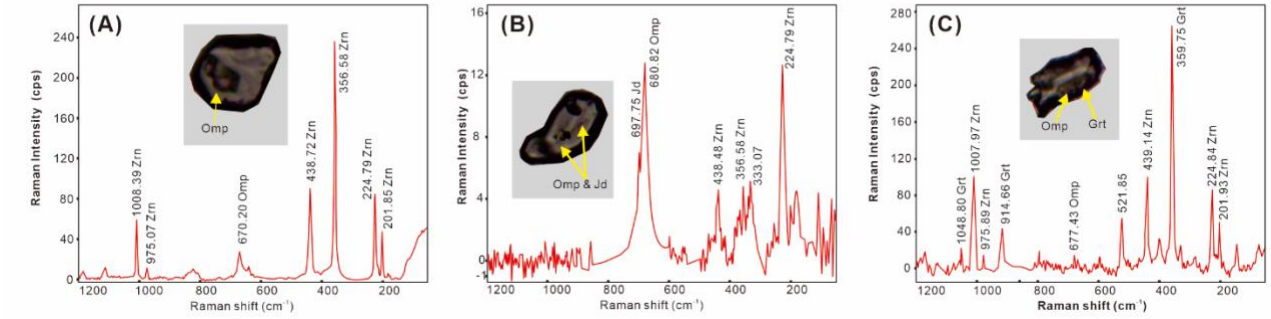

Figure 10. Raman spectra of (A) omphacite (Omp) inclusions, (B) omphacite/jadeite inclusions, and (C) garnet (Grt) and omphacite inclusions in Group #2 zircon (Zrn) grains from the Nuomuhong retrograde eclogite, middle East Kunlun orogen.

DISCUSSION

Constraints on the Timing of Metamorphism

Two distinct metamorphic age groups of 464±9 Ma (MSWD=0.5) and 419±4 Ma (MSWD=1.3) were obtained from the Nuomuhong eclogites (Figs. 9) . The first-group zircons possess core–rim structures with broad zoning and core contrast brightness suggestive of potential residual metamorphic zircons. Though most of the zircons from these two groups yielded low Th/U ratios, the first group shows a progressive increase in HREE patterns from Dy to Lu (Fig. 9D). We

interpret the first group of zircon age to approximate the age of eclogite protoliths, which is similar to the 520–460 Ma age inferred for regional ophiolite formation in this setting (Qi et al., 2016c) and the 471–454 Ma magmatic events of Proto-Tethys oceanic crust subduction (Fu et al., 2022b).

In contrast, the second-group zircons have typical morphological and textural characteristics of metamorphic zircons (Wu and Zheng, 2004), with similarly extremely low Th/U ratios (Table S8). During metamorphic recrystallization, Th is more likely to be expelled from the zircon lattice than U, accounting for the relatively low Th/U ratios observed. Laser Raman spectroscopy analyses of the inclusions in the second-group zircons reveals the presence of typical eclogite facies minerals like omphacite and garnet, indicating a younger age for the Group #2 zircons compared to peak-pressure metamorphism. The nearly flat HREE patterns further suggests these zircons grew in relatively high-pressure conditions in the presence of garnet (Fig. 9D). Therefore, we interpret the younger 419±4 Ma age as the lower age limit for peak eclogite facies metamorphism. This age is consistent with previously reported (near) peak ages of 428–411 Ma for eclogites in other localities in the EKOB (Bi et al., 2020; Guo et al., 2020; Jia et al., 2014; Meng et al., 2013b; Pan and Zhang, 2020; Qi et al., 2014; Qi et al., 2016b; Song et al., 2018b; Tang et al., 2022; Wang et al., 2012; Wang, 2020). In summary, our SHRIMP zircon U-Pb data suggest that the protoliths of the Nuomuhong eclogites could have been formed at ~464 Ma, after which they experienced eclogite facies metamorphism prior to 419±4 Ma, coincident with protolith and metamorphic ages from regional EKOB eclogites.

Tectonic Affinity of Protoliths of the Eclogites

Although eclogites may undergo complex prograde and retrograde metamorphic processes, the

study of eclogites in many orogenic belts indicate that the activity of external fluids did not cause obvious element migration, especially for the HFSE and REE (Wang et al., 2013a). In this study, the low loss on ignition of <0.38 and the relatively coherent patterns in the normalized REE and trace element diagrams (Figs. 8A and 8B), suggest limited modification of most elements in the Nuomuhong eclogites. Here we use the fluid-immobile elements to fingerprint the tectonic protoliths of the Nuomuhong eclogites.

The Nuomuhong eclogites have low SiO_2 in the range of 48.57–51.07 wt.%, and moderate 1.04–1.32 wt.% TiO_2, 6.43–8.77 wt.% MgO and 154–290 ppm Cr contents, similar to tholeiitic basalts. In the normalized REE and trace element diagrams, most of the eclogite samples have near-flat and slightly enriched LREE, a characteristic reminiscent of N-MORB and E-MORB (Figs. 8A and 8B). The low Zr/Y ratios preclude an intra-plate origin, as supported by the Zr vs. Zr–Y cross plot (Fig. 11A). Tectonic discrimination utilizing exemplary HFSEs and REEs such as Nb, Ta, La, Ce, Yb and Y, allude to a majority of the samples converging on E-MORB and N-MORB within the MORB–OIB array (Figs. 11B-D), an indication of their derivation from MORB-type oceanic crust. These observations demonstrate that the protoliths of the Nuomuhong eclogites are essentially subducted MORB-like oceanic crust basalt or gabbro, similar to oceanic crust-derived eclogites in the eastern segment of the EKOB locality (Song et al., 2018b).

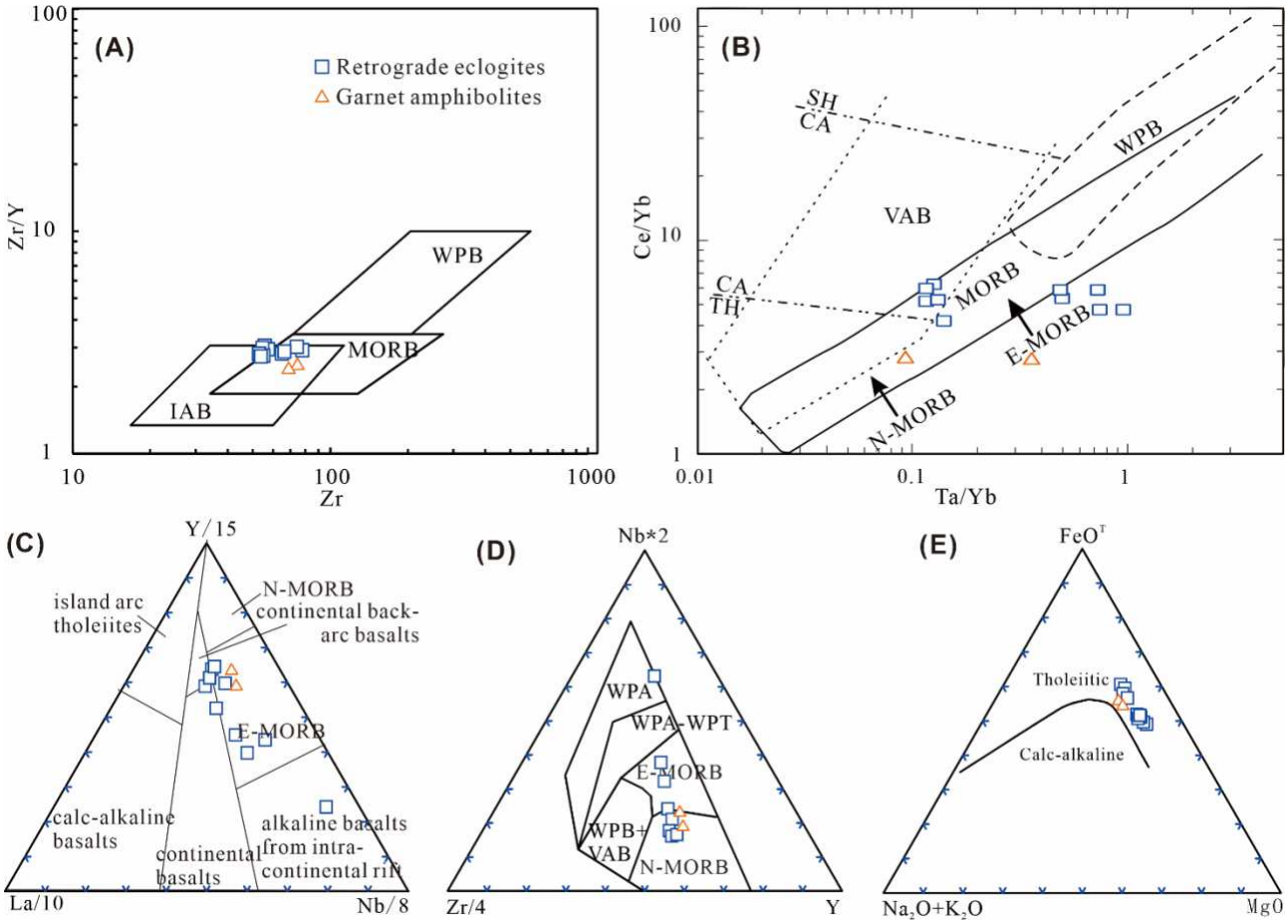

Figure 11. Tectonic discrimination diagrams (A–D) for the retrograde eclogite. (A) Zr–Zr/Y diagram (Pearce and Norry, 1979); (B) Ce/Yb–Ta/Yb diagram (Pearce, 1982); (C) Y–La–Nb diagram (Cabanis and Lecolle, 1989); (D) Nb–Zr–Y diagram (Meschede, 1986); (E) AFM diagram (Irvine and Baragar, 1971). W corresponds to CA–calc-alkaline, MORB–mid-ocean ridge basalt, SH–shoshonitic, TH–tholeiitic, VAB–volcanic arc basalt, WPB–within plate basalt.

Metamorphic records for the oceanic subduction and continental collision in the northern Proto-Tethys

Based on petrographic observations, conventional geothermobarometry and phase equilibrium modelling, five metamorphic stages and associated *P–T* conditions were determined for the Nuomuhong eclogites, namely: (1) the prograde M_1 stage with *P–T* conditions of >14.0 kbar/~470–

506°C; (2) the peak-*P* M_2 eclogite facies stage at ~26 kbar P and ~570°C T; (3) the early M_3 retrograde high-*P* granulite facies stage; (4) the subsequent (M_4 retrograde medium-*P* granulite facies stage with peak *T* at ~860–900°C at 6 kbar; and (5) the later M_5 retrograde amphibolite facies stage at <6.2 kbar P and ~710–730°C T. These *P–T* estimates define a clockwise *P–T* path characterized by heating decompression from the *Pmax* stage of eclogite facies formation to the *Tmax* stage for the granulite facies, followed by a final decompressional cooling stage to amphibolite facies (Fig. 12).

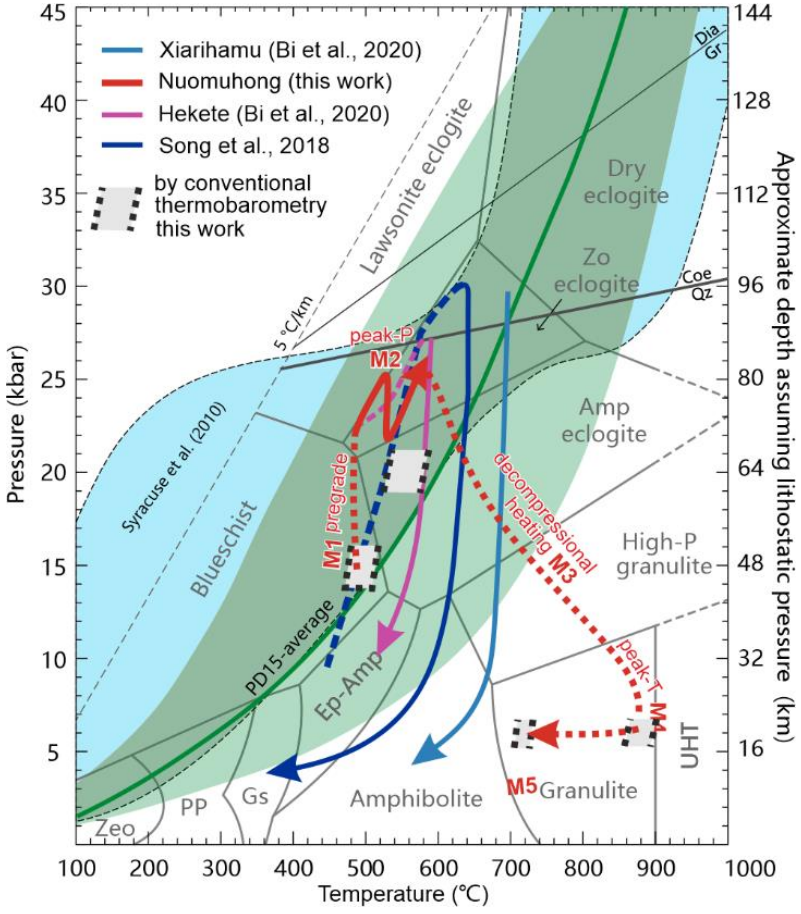

Figure 12. The *P–T* path for the Nuomuhong eclogite in this study, compared with eclogite in the eastern segment of the East Kunlun orogen from Song et al. (2018b). Boundaries for various metamorphic facies, High-P granulite, UHT metamorphic facies according to Schreyer (1988), Syracuse et al. (2010), and Maruyama et al. (1996). Abreviations and phase equilibria are after Liou et al. (2004).

As already mentioned, the protoliths of the eclogite lithologoes are interpreted to be subducted MORB-type oceanic crust, a fossil of the East Kunlun branch of the Proto-Tethys Ocean. The metamorphic change from M_1 prograde to M_2 peak-*P* eclogite facies at pressures of up to ~26 kbar, indicates that the oceanic crust was subducted down to ~83 km (Fig. 13A). This conclusion considers a lithostatic pressure of 1 kbar ≈ 3.2 km, where the eclogites underwent subduction zone *HP* metamorphism. The estimated *P–T* conditions for the peak-*P* stage Nuomuhong eclogites, corresponding to an apparent thermal gradient of ~220 °C/GPa, is a typical feature of generalized <375 °C/GPa low *T/P* geothermal subduction zones (Xia et al., 2022a). Locally, subduction of the oceanic crust under UHP condition resulted in the production of the coesite pseudomorphs recorded in the eastern EKOB rocks (Bi et al., 2018; Song et al., 2018b). Phase equilibrium modelling suggests that both the core and garnet rim minerals suggest a two phase increase in pressure and temperature conditions that ended with a reversed drop in pressure (Fig. 13C),. The decompression process likely records a failed exhumation attempt that was followed by further burial, as demonstrated by the second segment of prograde evolution. In subduction channels, HP/UHP rock-bearing mélanges formed and evolved with different fates, including 1) successful exhumation to a shallow level accretionary complex, or 2) failed exhumation and subduction into the mantle. Multiple cycles of *P* increase during a single orogenic event, interpreted to represent burial-partial exhumation cycles, have been reported in eclogite from the Alps (Rubatto et al., 2011), western Dabie (Xia et al., 2022b) and the western Tianshan (Li et al., 2016) HP/UHP orogens. These cycles could have arisen because of convective flow in the subduction channel (Zheng et al., 2012). Therefore, M_1 and M_2 metamorphism of the Nuomuhong eclogites preserve thermal state history of

537 a Proto-Tethyan subduction zone and a complicated account of a Proto-Tethyan ocean crust
538 subduction event during accretionary orogenesis.

539 The peak-*P* stage was followed by M_3 retrograde high-*P* granulite facies metamorphism and M_4
540 medium-*P* granulite facies, characterized by the symplectite Cpx II + Pl II rimming Cpx I_b, and the
541 symplectite Opx + Pl II rimming Cpx II. The calculated peak temperatures of ~860–900°C at ~6
542 kbar indicate that eclogite was exhumed to the middle crust level, undergoing decompressional
543 heating in the process. The high *T* metamorphic overprint on eclogite has not been recognized in
544 other localities in the EKOB, implying that the Nuomuhong eclogite may have stayed in the middle
545 crust for a sustained amount of time before final exhumation to the Earth surface. Such a situation
546 was recently recognized in southern Tibet (Wang et al., 2021), where high-*T* overprinting of
547 eclogite facies is regarded as metamorphic evidence of initial to mature stage continental collision.
548 During the maturation of continental collision, the structural, magmatic, and metamorphic response
549 changes significantly in the orogen. Firstly, the orogenic belt significantly thickens due to tectonic
550 compression and continuous subduction of the down going continental lithosphere. Secondly, the
551 subducting oceanic slab breaks off, leading to the buoyant exhumation of the deeply subducted
552 continental crust to the middle-shallow level. In some circumstances, the change of geometry of
553 orogenic wedges, experienced in mainly foreland basin sequences, accretionary and arc complexes,
554 hampers the exhumation of HP/UHP rocks, resulting to persistence in the middle crust. In addition,
555 slab break-off and crustal thinning promoted by upwelling of the asthenosphere, results in the
556 eventual underplating of a large volume of mafic magma in the lower crust, leading to intense
557 partial melting of crustal rocks and the generation of collision-related felsic magmatism. The
558 underplating during collision-related magmatism acts as a potential heat source for the high-*T*

559 metamorphism that overprints previously exhumed HP/UHP metamorphic rocks (Fig. 13B).
560 Therefore, the Nuomuhong eclogites preserve a long-term record for early subduction-accretionary
561 to later collisional orogenesis.
562
563 **Implications for the evolution of the East Kunlun branch of the Proto-Tethys Ocean**
564 In the Qilian–Qaidam–Kunlun area along the northern margin of the Tibetan Plateau, several
565 Early Paleozoic sutures separating microcontinental blocks and/or arc terranes were distributed
566 between the northern Gondwana and combined Tarim–North China cratons, terminating in the
567 ultimate closure of the Proto-Tethys Ocean (Fu et al., 2022a; Li et al., 2018c; Song et al., 2018a;
568 Zhao et al., 2018). The remnants of the Proto-Tethys Ocean preserved in northern Tibet can be
569 divided into the Qilian Ocean and North Qilian backarc in the north, the South Qilian Ocean in the
570 middle, and the East Kunlun Ocean in the south, separated by the Central Qilan and Qaidam blocks
571 (Fig. 13D), respectively (Song et al., 2018a). The detailed evolutionary history from continental
572 rifting during the break of Rodinia, oceanic subduction-accretion, terrane accretion/collision and
573 final continental collision, remains debated (Fu et al., 2019; Fu et al., 2018; Song et al., 2018b;
574 Song et al., 2014; Wu et al., 2021; Wu et al., 2020; Wu et al., 2019; Xiao et al., 2009; Zuza et al.,
575 2017). The EKOB contains complex geological units related to continental rifting, oceanic
576 subduction and continental collision, providing an excellent window for evidencing the evolution of
577 the Proto-Tethys Ocean and associated orogenesis (Song et al., 2018b).

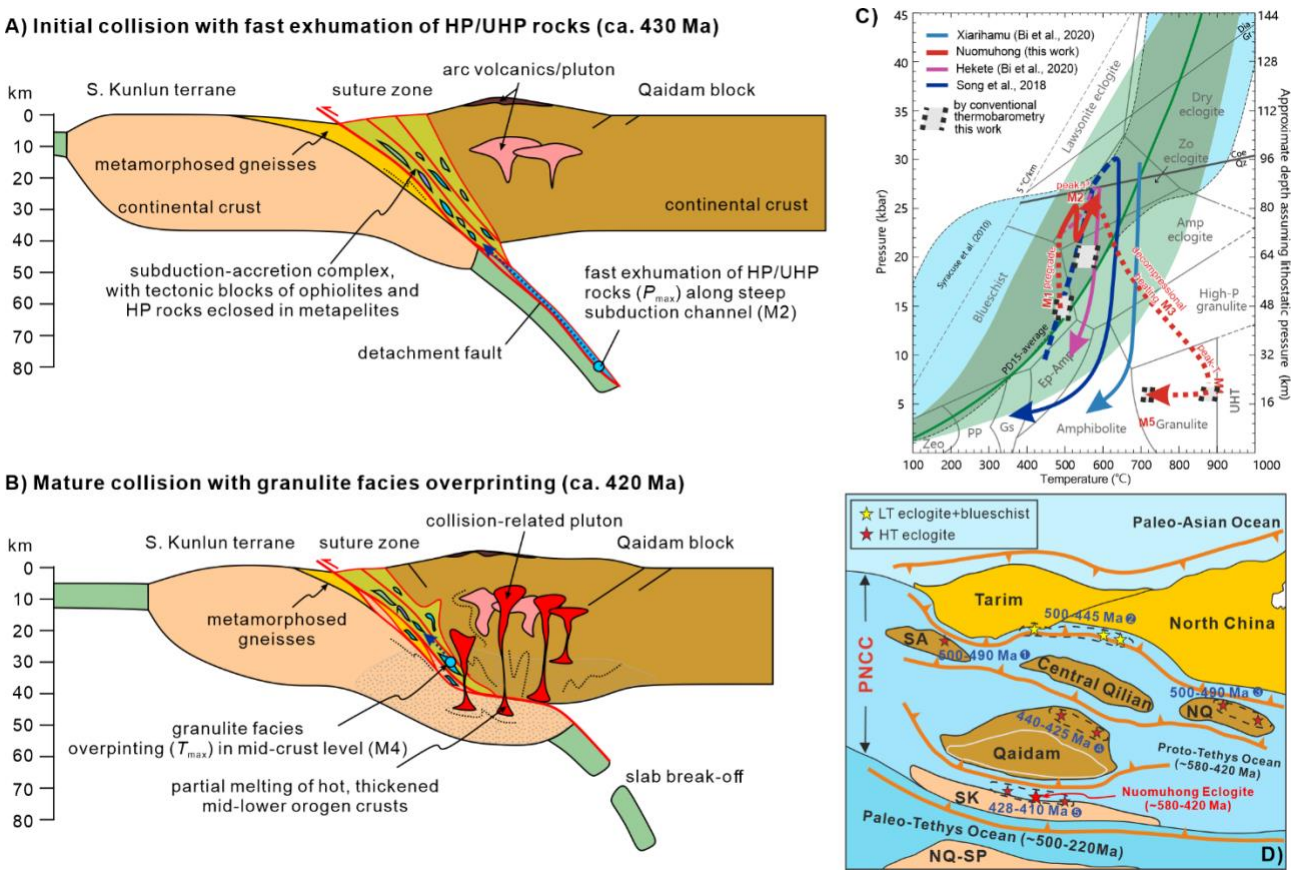

Figure 13. Tectonic model for the Eastern Kunlun orogen and the Proto-Tethys Ocean.

The continental rifting, supported by meta-gabbro in the south Jinshuikou Group in East Kunlun, yielded 796±41Ma formation age (Ren et al., 2011). These data suggest that the East Kunlun began breaking up no later than 796±41Ma, the Qingshuiquan ophiolite at 522±4 Ma and 518±3 Ma, the Tatuo ophiolite at 522±3 Ma, and the Buqingshan Delisitai MOR-ophiolite at 516±6 Ma (Liu et al., 2011b). The Early Paleozoic 535±10 Ma MOR-gabbro in the Maji Mountain area (Li, 2008), contains ample evidence for the formation of the East Kunlun oceanic crust (Lu et al., 2002; Yang et al., 1996). Subsequently, during the start of the late-Cambrian, the Kunlun Ocean began to subduct northward, with a series of magmatic and metamorphic events associated with this subduction event. The 507±8 Ma Qingshuiquan granulite in the central East Kunlun Suture zone and the 480±3 Ma Yaziquan island-arc diorite in the Qimantag Mountains (Cui et al., 2011; Li et al.,

591 2006), are an expression of these magmatic and metamorphic activities in the center and North
592 Kunlun areas. Moreover, the time of formation of the 515±4 Ma quartz diorite in the Kekesha area
593 in Dulan, signifies the start of ocean basin subduction (Zhang et al., 2010b). During this time, the
594 East Kunlun area stretched into several extensional oceanic or back-arc basins, as the oceanic crust
595 was in a state of continuous expansion (Qi et al., 2016a).

596 From the late Ordovician to the early Silurian, the uninterrupted extension and distribution of
597 back-arc basins in the Central East Kunlun zone continued with persistent and abundant magmatic
598 activity (Chen et al., 2016). This conclusion is exemplified by the distribution of 448±4 Ma
599 basaltic-dacitic lavas near Central East Kunlun, including the deposition of the Bairiqiete
600 intermediate acidic rock suite that formed island-arc granodiorites marked by the 441±6 Ma and the
601 438±3 Ma island-arc rhyolite porphyry, the 440±6 Ma Yikehalaer granodiorites of typical adakite
602 geochemical characteristics (Li et al., 2014; Liu et al., 2011a), the 447 ± 9 Ma metamorphosed
603 diorite in the southern Xiangride area and the 450±4 Ma rhyolite in the Nachita Group (Zhang et al.,
604 2010c) . The diagenesis of arc magma occurred in response to oceanic crust subduction, while the
605 445±5 Ma SHRIMP ages for the Dagele ophiolite gabbro probably denote the ultimate subduction
606 of the Proto-Tethys oceanic crust (Du et al., 2017).

607 After middle-late Silurian, final closure of the Kunlun branch of the Proto-Tethys Ocean,
608 resulted into continental subduction and collisional orogeny. The high angle thrust nappe
609 deformation in the East Kunlun Fault zone records a 426–408 Ma age for this event (Wang et al.,
610 2003b), and marks the disappearance of the island arc environment alongside contemporaneous
611 early Paleozoic collisional orogenic activity. There are a great deal of medium-late Silurian to early
612 Devonian collisional granites (Li et al., 2013; Liu et al., 2012). These granites are typified by the

425±7 Ma Helegangnaren A-type alkali feldspar granite, the 407±3 Ma Yuejinshan granodiorite, the 423±5 Ma syn-collisional granite from the Changshishan mélange belt, distributed between the north Kunlun and the southern margin of the Qaidam block. Collectively, these lithologies are identical with this tectonic environment, while the presence of the 428–411 Ma Nuomuhong eclogite and others in the East Kunlun record the ensuing continental subduction and collisional orogeny.

We propose that when the Kunlun Ocean crust subducted towards the north and under the southern margin of the Qaidam Block during the Early Paleozoic before 440 Ma, the continental basaltic protolith of the East Kunlun eclogites formed in a continental margin setting, were impacted by oceanic crust subduction. The high-amphibolite to granulite facies metamorphism owing to tecto-thermal events of oceanic crust subduction, is associated with the prograde minerals assemblage of the Nuomuhong eclogites and the 460 Ma Jinshuikou Group gneissic lithologies (Zhang et al., 2003). After the early Silurian continental subduction and collisional orogeny closure of the Proto-Tethys Ocean, the protolith of the Jinshuikou Group basement mafic rocks were buried down to >100 km depth in the subduction channel. Evidence of HP-UHP metamorphism, in addition to the eclogite facies, is supported by the intercalation of the country rocks with eclogites (Bi et al., 2020).

When the East Kunlun orogenic belt began its post-collisional extension in the middle-late Silurian, the eclogites were exhumed onto the shallow crust. The slight 430–411 Ma timing gap for the accumulation of these eclogites in East Kunlun (Meng et al., 2013b; Qi et al., 2014; Qi et al., 2016a; Song et al., 2018b), is probably attributed to uneven timing and speed of exhumation in different parts of the enormous orogenic belt, accompanied by internal asymmetric subduction

635 suturing (Bi et al., 2022), evidenced by eclogites in the eastern and western Kunlun outcrops.
636 Eventually the molasse sedimentary assemblage of the Devonian Maoniushan group signified the
637 end of the early Paleozoic Proto-Tethys Ocean tectonic cycle in East Kunlun and the beginning of
638 the new cycle of ocean-continental evolution associated with the North Paleo-Tethys Ocean (Chen
639 et al., 2008b; Li et al., 2013).

640 The discovery of the Nuomuhong eclogite constrained the timing of transition from continental
641 subduction to collision in the early Devonian and formed a super HP-UHP metamorphic belt with
642 other eclogite outcrops in the EKOB block. This assemblage represents an excellent example of an
643 early Paleozoic continental convergence boundary between the Qaidam Block and the East Kunlun
644 Massif, which is of great significance for furthering the understanding, formation, and evolution of
645 the Proto-Tethys system.

646

647 **CONCLUSION**

648 (1) Retrograde eclogites with garnet and omphacite formed during partial tectonic
649 decompression, characterizes the Nuomuhong area in the eastern part of the East Kunlun orogenic
650 belt. The retrograde eclogites underwent prograde, eclogite, HP granulite, granulite, and
651 amphibolite facies metamorphisms, along a *P–T* clockwise pathway: (1) the M1 prograde stage with
652 P–T conditions of >14.0 kbar/~470–506°C; (2) the peak-P eclogite facies stage (M2, ~26
653 kbar/~570°C); (3) the early retrograde high-P granulite facies stage (M3); (4) the subsequent
654 retrograde high-T granulite facies stage (M4) with peak T at ~860–900°C at a pressure of 6 kbar;
655 and (5) the later retrograde amphibolite facies stage (M5, < 6.2 kbar/~710–730°C). The
656 orthopyroxene associated with eclogite in EKOB revealed that the Nuomuhong eclogites

experienced granulite metamorphism different from the other eclogites in EKOB.

(2) The protolith of the Nuomuhong eclogite with slight LREE enrichment has MOR basalt-like geochemical signatures. Zircon U–Pb analyses and Ranman spectrometer show the peak metamorphism or early exhumation formed at 419 ± 4 Ma (MSWD=1.3). The zircon cores ages yielding 464 ± 4 Ma (MSWD=0.5) recorded the protolith ages of Nuomuhong eclogite rather than the Middle Ordovician tectonic-thermal events associating with the metamorphic ages of Jinshuikou Group.

(3) The oceanic crust of East Kunlun Ocean, the southern part of Proto-Tethys Ocean, formed before the middle Cambrian and began to subduct northward after initial late-Cambrian. From the late Ordovician to the early Silurian, the back-arc basins distributing along the Central East Kunlun continued extending with abundant magmatic activities. After middle-late Silurian, the Kunlun Ocean, a branch of Proto-Tethys Ocean, had closed finally and transformed into the continental subduction and collisional orogeny. The presence of Nuomuhong eclogite and other eclogites (428–411 Ma) in East Kunlun also recorded the continental subduction and collisional orogeny. Finally, the later Devonian molasse sedimentary assemblage represented the end of the Proto-Tethys evolution and the beginning of Paleo-Tethys evolution in East Kunlun. The discovery of Nuomuhong eclogite formed a HP-UHP metamorphism belt with other eclogite dew points in East Kunlun.

ACKNOWLEDGEMENTS

Financial support for this study was jointly provided by the National Natural Science Foundation of China (Grant No. 41703024, 42102244, 4210268), the China Geological Survey

679 Project (Grant No. 1212010510507 and DD20221814) and the China Scholarship Council (Grant
680 No. 201906415032). We give our thanks to Profs. Tim Kusky and Lu Wang for their constructive
681 suggestions and helpful comments to improve this manuscript.
682

REFERENCES

Bi, H., Song, S., Dong, J., Yang, L., Qi, S., and Allen, M. B., 2018, First discovery of coesite in eclogite from East Kunlun, northwest China: Science Bulletin, v. 63, no. 23, p. 1536-1538.

Bi, H., Whitney, D., Song, S., and Zhou, X., 2022, HP–UHP eclogites in the East Kunlun Orogen, China: P–T evidence for asymmetric suturing of the Proto-Tethys Ocean: Gondwana Research, v. 104, p. 199-214.

Bi, H. Z., Song, S. G., Yang, L. M., Allen, M. B., Qi, S. S., and Su, L., 2020, UHP metamorphism recorded by coesite-bearing metapelite in the East Kunlun Orogen (NW China): Geological Magazine, v. 157, no. 2, p. 160-172.

Bingen, B., Davis, W. J., and Austrheim, H., 2001, Zircon U-Pb geochronology in the Bergen arc eclogites and their Proterozoic protoliths, and implications for the pre-Scandian evolution of the Caledonides in western Norway: Geological Society of America Bulletin, v. 113, no. 5, p. 640-649.

Cabanis, B., and Lecolle, M., 1989, Le diagramme La/10Y/15Nb/8: un outil pour la discrimination des sries volcaniques et la mise en vidence des procsses de mlange et/ou de contamination crus-tale: CR Acad. Sci., Sr, v. 2, p. 2023-2029.

Chen, J. J., Fu, L. B., Wei, J. H., Tian, N., Xiong, L., zhao, Y. J., and Qi, Y. Q., 2016, Geochemical characteristics of Late Ordovician granodiorite in Gouli Area, Eastern Kunlun Orogenic Belt, Qinghai Province: Implications on the Evolution of Proto-Tetys Ocean.: Earth Science, v. 41, no. 11, p. 1863-1882.

Chen, N., Sun, M., Wang, Q., Zhang, K., Wan, Y., and Chen, H., 2008a, U-Pb dating of zircon from the Central Zone of the East Kunlun Orogen and its implications for tectonic evolution: Science in China Series D: Earth Sciences, v. 51, no. 7, p. 929-938.

Chen, N. S., Sun, M., Wang, Q. Y., Zhang, K. X., Wan, Y. S., and Chen, H. H., 2008b, Zircon U-Pb dating and tectonic evolution implications in the central belt of East Kunlun Orogenic Belt SCIENCE CHINA Earth Sciences, v. 38, no. 6, p. 657-666.

705 Chen, X., Xu, R. K., Zheng, Y. Y., Wang , Y. K., Wang, H. J., Bai, J., Du, W. Y., and Lu, R., 2015, The determination of peak
706 temperature of eclogites in the west of Tieshiguan area, North Qaidam UHP of Qinghai Province, and its
707 geological significance: Geological Bulletin of China, v. 34, no. 12, p. 2292-2301.
708 Chen, Y. X., Pei, X. Z., Li, R. B., Liu, Z. Q., Li, Z. C., zhang, X. F., Chen, G. C., Liu, Z. G., Ding, S., and Guo, J., 2011, Zircon U-
709 Pb Age of Xiaomiao Formation of Proterozoic in the Eastern Section of the East Kunlun Orogenic Belt:
710 GEOSCIENCE, v. 25, no. 3, p. 510-521.
711 Coleman, R. G., Lee, D. E., Beatty, L. B., and Brannock, W. W., 1965, Eclogites and Eclogites: Their Differences and
712 Similarities: Geological Society of America Bulletin, v. 76, no. 5, p. 483.
713 Corfu, F., Hanchar, J. M., Hoskin, P. W. O., and Kinny, P., 2003, Atlas of Zircon Textures: Reviews in Mineralogy and
714 Geochemistry, v. 53, no. 1, p. 469–500.
715 Cui, M. H., Meng, F. C., and Wu, X. K., 2011, Early Ordovician island arc of Yaziquan, west of Qimantag Mountain, East
716 Kunlun: evidences from geochemistry, Sm-Nd isotope and geochronology of intermediate-basic rocks: Acta
717 Petrologica Sinica v. 27, no. 11, p. 3365-3379.
718 Dobretsov, N. L., 1991, Blueschists and eclogites: a possible plate tectonic mechanism for their emplacement from the
719 upper mantle: Tectonophysics, v. 186, no. s3–4, p. 253–268.
720 Dong, Y. P., He, D. F., Sun, S. S., Liu, X. M., Zhou, X. H., Zhang, F. F., Yang, Z., Cheng, B., Zhao, G. C., and Li, J. H., 2018,
721 Subduction and accretionary tectonics of the East Kunlun orogen, western segment of the Central China
722 Orogenic System: Earth-Science Reviews, v. 186, p. 231-261.
723 Du, W., Jiang, C., Xia, M., Xia, Z., Zhou, W., Ling, J., Wang, B., and Yu, S., 2017, A newly discovered Early Paleozoic
724 ophiolite in Dagele, Eastern Kunlun, China, and its geological significance: Geological Journal, v. 52, p. 425-435.
725 Feng, D., Wang, C., Song, S., Xiong, L., Zhang, G., Allen, M. B., Dong, J., Wen, T., and Su, L., 2023, Tracing tectonic
726 processes from Proto- to Paleo-Tethys in the East Kunlun Orogen by detrital zircons: Gondwana Research, v.

115, p. 1-16.

Fu, C. L., Yan, Z., Guo, X. Q., Niu, M. L., Cao, B., Wu, Q., Li, X., and Wang, Z. Q., 2019, Assembly and dispersal history of continental blocks within the Altun-Qilian-North Qaidam mountain belt, NW China: International Geology Review, v. 61, no. 4, p. 424-447.

Fu, D., Huang, B., Johnson, T. E., Wilde, S. A., Jourdan, F., Polat, A., Windley, B. F., Hu, Z., and Kusky, T., 2022a, Boninitic blueschists record subduction initiation and subsequent accretion of an arc–forearc in the northeast Proto-Tethys Ocean: Geology, v. 50, no. 1, p. 10-15.

Fu, D., Kusky, T., Wilde, S. A., Polat, A., Huang, B., and Zhou, Z., 2018, Early Paleozoic collision-related magmatism in the eastern North Qilian orogen, northern Tibet: A linkage between accretionary and collisional orogenesis: GSA Bulletin, v. 131, no. 5-6, p. 1031-1056.

Fu, L., Bagas, L., Wei, J., Chen, Y., Chen, J., Zhao, X., Zhao, Z., Li, A., and Zhang, W., 2022b, Growth of early Paleozoic continental crust linked to the Proto-Tethys subduction and continental collision in the East Kunlun Orogen, northern Tibetan Plateau: GSA Bulletin.

Green, E. C. R., White, R. W., Diener, J. F. A., Powell, R., Holland, T. J. B., and Palin, R. M., 2016, Activity-composition relations for the calculation of partial melting equilibria in metabasic rocks: Journal of Metamorphic Geology, v. 34, no. 9, p. 845-869.

Guo, F., Wang, P., Wang, Z., and Feng, N., 2020, Geochemical and geochronology characteristics of retrograde eclogite in Xiarihamu area, East Kunlun Mountains, and its geological implications: Sedimentary Geology and Tethyan Geology, v. 40, no. 4, p. 45-55.

Han, L., Zhang, L., and Zhang, G., 2015, Ultra-deep subduction of Yematan eclogite in the North Qaidam UHP belt, NW China: Evidence from phengite exsolution in omphacite: American Mineralogist, v. 100, no. 8-9, p. 1848-1855.

He, D. F., Dong, Y. P., Liu, X. M., Yang, Z., Sun, S. S., Cheng, B., and Li, W., 2016, Tectono-thermal events in East Kunlun,

749 Northern Tibetan Plateau: Evidence from zircon U–Pb geochronology: Gondwana Research, v. 30, p. 179-190.
750 Hermann, J., 2002, Allanite: Thorium and light rare earth element carrier in subducted crust: Chemical Geology, v. 192,
751 no. 3, p. 289-306.
752 Hertgen, S., Yamato, P., Morales, L., and Angiboust, S., Brittle/Ductile deformation at depth during continental crust
753 eclogitization (Mont-Emilius klippe, Western Internal Alps), *in* Proceedings EGU General Assembly
754 Conference2016, Volume 18.
755 Holland, T., and Blundy, J., 1994, Non-ideal interactions in calcic amphiboles and their bearing on amphibole-
756 plagioclase thermometry: Contributions to Mineralogy and Petrology, v. 116, no. 4, p. 433-447.
757 Holland, T. J. B., and Powell, R., 2011, An improved and extended internally consistent thermodynamic dataset for
758 phases of petrological interest, involving a new equation of state for solids: Journal of metamorphic Geology, v.
759 29, no. 3, p. 333-383.
760 Irvine, T. N., and Baragar, W. R. A., 1971, A Guide to the Chemical Classification of the Common Volcanic Rocks:
761 Canadian Journal of Earth Sciences, v. 8, no. 5, p. 523-548.
762 Jia, L. H., Meng, F. C., and Feng, H. B., 2014, Fluid activity during eclogite-facies peak metamorphism：Evidence from a
763 quartz vein in eclogite in the East Kunlun, NW China: Acta Petrologica Sinica, v. 30, no. 8, p. 2339-2350.
764 Jiang, C. F., Yang, J. S., Feng, B. G., Zhu, Z. Z., Zhao, M., Chai, Y. C., Shi, X. D., Wang, H. D., and Hu, J. Q., 1992, Opening-
765 Closing Tectonics of Kunlun Mountains, Beijing, Geological Publishing House Geol. Memo. Series 5.
766 Klonowska, I., Janák, M., Majka, J., Froitzheim, N., and Kośmińska, K., 2016, Eclogite and garnet pyroxenite from Stor
767 Jougdan, Seve Nappe Complex, Sweden: implications for UHP metamorphism of allochthons in the
768 Scandinavian Caledonides: Journal of Metamorphic Geology, v. 34, no. 2, p. 103-119.
769 Leake, B. E., Woolley, A. R., Arps, C. E., Birch, W. D., Gilbert, M. C., Grice, J. D., Hawthorne, F. C., Kato, A., Kisch, H. J.,
770 and Krivovichev, V. G., 1997, Nomenclature of amphiboles; report of the Subcommittee on Amphiboles of the

771 International Mineralogical Association Commission on new minerals and mineral names: Mineralogical
772 magazine, v. 61, no. 405, p. 295-310.
773 Leake, B. E., Woolley, A. R., Birch, W. D., Burke, E. A., Ferraris, G., Grice, J. D., Hawthorne, F. C., Kisch, H. J., Krivovichev,
774 V. G., and Schumacher, J. C., 2004, Nomenclature of amphiboles: additions and revisions to the International
775 Mineralogical Association's amphibole nomenclature: Mineralogical Magazine, v. 68, no. 1, p. 209-215.
776 Li, B. S., Yan, M. D., Zhang, W. L., Fang, X. M., Yang, Y. P., Zhang, D. W., Chen, Y., and Guan, C., 2018a, Paleomagnetic
777 Rotation Constraints on the Deformation of the Northern Qaidam Marginal Thrust Belt and Implications for
778 Strike-Slip Faulting Along the Altyn Tagh Fault: Journal of Geophysical Research: Solid Earth, v. 123, no. 9, p.
779 7207-7224.
780 Li, H. K., Lu, S. N., Xiang, Z. Q., Zhou, H. Y., Guo, H., Song, B., Zheng, J. K., and Gu, Y., 2006, SHRIMP U-Pb zircon age of
781 the granulate from the Qingshuiquan area, Central Eastern Kunlun Suture Zone: Earth Science Frontiers, v. 13,
782 no. 6, p. 311-321.
783 Li, J., Gao, J., and Wang, X., 2016, A subduction channel model for exhumation of oceanic-type high-pressure to
784 ultrahigh-pressure eclogite-facies metamorphic rocks in SW Tianshan, China: Science China Earth Sciences, v.
785 59, no. 12, p. 2339-2354.
786 Li, R. B., Pei, X. Z., Li, Z. C., Chen, G. C., Liu, C. J., Chen, Y. X., Liu, Z. Q., and Pei, L., 2014, Age, Geochemical
787 Characteristics and Tectonic Significance of Yikehalaer Granodiorite in Buqingshan Tectonic Mélange Belt,
788 Southern Margin of East Kunlun: Acta Geoscientia Sinica, v. 4, p. 434-444.
789 Li, R. B., Pei, X. Z., Li, Z. C., Pei, L., Chen, G. C., Wei, B., Chen, Y. X., Liu, C. J., and Wang, M., 2018b, Cambrian (~ 510 Ma)
790 ophiolites of the East Kunlun orogen, China: A case study from the Acite ophiolitic tectonic mélange:
791 International Geology Review, v. 60, no. 16, p. 2063-2083.
792 Li, R. B., Pei, X. Z., Li, Z. C., Sun, Y., Pei, L., Chen, G. C., Chen, Y. X., Liu, C. J., and Wei, F. H., 2013, Regional Tectonic

793 Transformation in East Kunlun Orogenic Belt in Early Paleozoic: Constraints from the Geochronology and
794 Geochemistry of Helegangnaren Alkali-feldspar Granite: ACTA GEOLOGICA SINICA English Edition, v. 87, no. 2,
795 p. 333-345.
796 Li, S. Z., Zhao, S. J., Liu, X., Cao, H. H., Yu, S., Li, X. Y., Somerville, I., Yu, S. Y., and Suo, Y. H., 2018c, Closure of the Proto-
797 Tethys Ocean and Early Paleozoic amalgamation of microcontinental blocks in East Asia: Earth-Science
798 Reviews, v. 186, p. 37-75.
799 Li, W. Y., 2008, Chronology and Geochemistry of ophiolite and Island arc magmatic rocks in West Qingling-East Kunlun
800 Orogenic Belt, Constraint for Tethys evolution [doctor: University of Science and Technology of China, 1-154 p.
801 Liou, J. G., Tsujimori, T., Zhang, R. Y., Katayama, I., and Maruyama, S., 2004, Global UHP Metamorphism and
802 Continental Subduction/Collision: The Himalayan Model: International Geology Review, v. 46, no. 1, p. 1-27.
803 Liu, B., Ma, C. Q., Zhang, J. Y., Xiong, F. H., Huang, J., and Jiang, H. A., 2012, Petrogenesis of Early Devonian intrusive
804 rocks in the east part of Eastern Kunlun Orogen and implication for Early Palaeozoic orogenic processes: Acta
805 Petrologica Sinica, no. 6, p. 1785-1807.
806 Liu, Q., Meng, F., Li, S., Feng, H., Jia, L., and Tian, G., 2016, Geochronology of zircon from the paragneiss of Kuhai Group
807 in southern East Kunlun terrane: ACTA PETROLOGICA ET MINERALOGICA, v. 35, no. 3, p. 15.
808 Liu, Z. Q., Pei, X. Z., Li, R. B., Li, Z. C., Chen, G. C., Chen, Y. X., Gao, J. M., Liu, C. J., Wei, F. H., Wang, X. L., and Zhang, G.,
809 2011a, Early Paleozoic intermediate-acid magmatic activity in Bairiqiete area along the Buqingshan tectonic
810 melange belt on the southern margin of East Kunlun:Constraints from zircon U-Pb dating and geochemistry:
811 Geology in China, v. 38, no. 5, p. 1150-1167.
812 Liu, Z. Q., Pei, X. Z., Li, R. B., Li, Z. C., Zhang, X. F., Liu, Z. G., Chen, Y. X., Chen, G. C., Ding, S. P., and Guo, J. F., 2011b, LA-
813 ICP-MS Zircon U-Pb Geochronology of the Two Suites of Ophiolites at the Buqingshan Area of the A'nyemaqen
814 Orogenic Belt in the Southern Margin of East Kunlun and 1ts Tectonic Implication: ACTA GEOLOGICA SINICA, v.

85, no. 2, p. 185-194.

Lu, L., Wu, H. Z., Hu, D. G., BAROSH, P. J., Hao, S., and C.J., Z., 2010, Zircon U-Pb age for rhyolite of the Maoniushan Formation and its tectonic significance in the East Kunlun Mountains: Acta Petrologica Sinica, v. 26, no. 4, p. 1150-1158.

Lu, S. N., Yu, H. F., Jin, W., Li, H. K., and Zheng, J. K., 2002, Microcontinents on the eastern margin of Tarim paleocontinent: Acta Petrologica et Mineralogica, v. 21, no. 4, p. 317-326.

Luo, Z. H., Deng, J. F., Cao, Y. Q., Guo, Z. F., and Mo, X. X., 1999, On Late Paleozoic-Early Mesozoic volcanism and regional tectonic evolution of eastern Kunlun, Qinghai Province: Geoscience, v. 13, no. 1, p. 51-56.

Maruyama, S., Liou, J., and Terabayashi, M. J. I. g. r., 1996, Blueschists and eclogites of the world and their exhumation, v. 38, no. 6, p. 485-594.

Meng, F., Cui, M., Wu, X., Wu, J., and Wang, J., 2013a, Magmatic and metamorphic events recorded in granitic gneisses from the Qimantag, East Kunlun Mountains, Northwest China: Acta Petrologica Sinica, v. 29, no. 6, p. 2107-2122.

Meng, F. C., Cui, M. H., Jia, L. H., Ren, Y. F., and Feng, H. B., 2015a, Paleozoic continental collision of the East Kunlun orogen: Evidence from protoliths of the eclogites: Acta Petrologica Sinica, v. 31, no. 12, p. 3581-3594.

Meng, F. C., Cui, M. H., Wu, X. K., and Ren, Y. F., 2015b, Heishan mafic–ultramafic rocks in the Qimantag area of Eastern Kunlun, NW China: Remnants of an early Paleozoic incipient island arc: Gondwana Research, v. 27, no. 2, p. 745-759.

Meng, F. C., Jia, L. H., Ren, Y. F., Liu, Q., and Duan, X. P., 2017, Magmatic and metamorphic events recorded in the gneisses of the Wenquan region, East Kunlun Mountains, Northwest China: Evidence from the zircon U-Pb geochronology: Acta Petrologica Sinica, v. 33, no. 12, p. 3691-3709.

Meng, F. C., Tian, G., Duan, X. P., Fan, Y., and Ren, Y., 2018, Evidence from Garnet for Genesis of Garnet-Cordierite-

837 Granite in the Jinshuikou Area, Eastern Segment of the East Kunlun Mountains: Bulletin of Mineralogy,
838 Petrology Geochemistry v. 37, no. 2, p. 192-204.
839 Meng, F. C., Yang, H. J., Makeyev, A. B., Ren, Y. F., Kulikova, K. V., and Bryanchaninova, N. I., 2016, Jadeitite in the Syum-
840 Keu ultramafic complex from Polar Urals, Russia: insights intofluid activity in subduction zones: European
841 Journal of Mineralogy, v. 28, no. 6, p. 1079-1097.
842 Meng, F. C., Zhang, J. X., and Cui, M. H., 2013b, Discovery of Early Paleozoic eclogite from the East Kunlun, Western
843 China and its tectonic significance: Gondwana Research, v. 23, no. 2, p. 825-836.
844 Meschede, M., 1986, A method of discriminating between different types of mid-ocean ridge basalts and continental
845 tholeiites with the Nb · 1bZr · 1bY diagram: Chemical geology, v. 56, no. 3-4, p. 207-218.
846 Mo, X. X., Luo, Z. H., Deng, J. F., Yu, X. H., Liu, C. D., Chen, H. W., and Liu, H. Y., 2007, Granitoids and Crustal Crowth in
847 the East Kunlun Orogenic Belt: Geological Journal of China Universities, v. 13, no. 3, p. 403-414.
848 Morimoto, N., 1988, Nomenclature of pyroxenes: Mineralogy & Petrology, v. 39, no. 1, p. 55-76.
849 Pan, T., and Zhang, Y., 2020, Geochemical Characteristics and Metallogenic Response of the Eclogite from Xiarihamu
850 Magmatic Ni-Cu Sulfide Deposit in Eastern Kunlun Orogenic Belt: Geotectonica et Metallogenia, v. 44, no. 3, p.
851 447-464.
852 Pearce, J. A., 1982, Trace element characteristics of lavas from destructive plate boundaries, *in* Thorpe, R. S., ed.,
853 Andesites: Orogenic Andesites and Related Rocks: Chichester, England, John Wiley & Sons, p. 528-548.
854 Pearce, J. A., and Norry, M. J., 1979, Petrogenetic implications of Ti, Zr, Y, and Nb variations in volcanic rocks:
855 Contributions to Mineralogy&Petrology, v. 69, no. 1, p. 33-47.
856 Qi, S. S., Song, S. G., Shi, L. C., Cai, H. J., and Hu, J. C., 2014, Discovery and its geological significance of Early Paleozoic
857 eclogite in Xiarihamu-Suhaitu area, western part of the East Kunlun: Acta Petrologica Sinica, v. 30, no. 11, p.
858 3345-3356.

Qi, X. P., Fan, X. G., Yang, J., Cui, J. T., Wang, B. Y., and Fan, Y. Z., 2016a, The discovery of Early Paleozoic eclogite in the upper reaches of Langmuri in eastern East Kunlun Mountains and its significance: Geological Bulletin of China, v. 35, no. 11, p. 1771-1783.

Qi, X. P., Fan, X. G., Yang, J., Cui, J. T., Wang, B. Y., and Fan, Y. Z., 2016b, The discovery of Early Paleozoic eclogite in the upper reaches of Langmuri in eastern East Kunlun Mountains and its significance: Geological Bulletin of China, v. 35, no. 11, p. 1771-1783.

Qi, X. P., Yang, J., Fan, X. G., Cui, J. T., Cai, Z. F., Zeng, X. W., Wei, W., Qu, X. X., and Zhai, Y. M., 2016c, Age, geochemical characteristics and tectonic significance of Changshishan ophiolite in central East Kunlun tectonic mélange belt along the east section of East Kunlun Mountains: Geology in China, v. 43, no. 3, p. 797--816.

Ravna, K., 2000, The garnet–clinopyroxene Fe2+–Mg geothermometer: an updated calibration: Journal of Metamorphic Geology, v. 18, no. 2, p. 211-219.

Ren, J. H., Zhang, K., Liu, Y. Q., Zhou, D. W., and Feng, Q., 2011, Geochemical characteristics and zircon dating of blasto-gabrro from the South Jinshuikou area,Eastern Kunlun: JOURNAL OF NORTHWEST UNIVERSITY(NATURAL SCIENCE EDITION), v. 41, no. 1, p. 100-106.

Rubatto, D., Regis, D., Hermann, J., Boston, K., Engi, M., Beltrando, M., and McAlpine, S. R. B., 2011, Yo-yo subduction recorded by accessory minerals in the Italian Western Alps: Nature Geoscience, v. 4, no. 5, p. 338-342.

Sajeev, K., Windley, B. F., Hegner, E., and Komiya, T., 2013, High-temperature, high-pressure granulites (retrogressed eclogites) in the central region of the Lewisian, NW Scotland: Crustal-scale subduction in the Neoarchaean: Gondwana Research, v. 23, no. 2, p. 526-538.

Schmidt, M. W., 1992, Amphibole composition in tonalite as a function of pressure: an experimental calibration of the Al-in-hornblende barometer: Contributions to Mineralogy&Petrology, v. 110, no. 2, p. 304-310.

Schorn, S., and Diener, J. F. A., 2017, Details of the gabbro-to-eclogite transition determined from microtextures and

881 calculated chemical potential relationships: Journal of Metamorphic Geology, v. 35, no. 1, p. 55-75.
882 Schreyer, W., 1988, Experimental studies on metamorphism of crustal rocks under mantle pressures: Mineralogical
883 Magazine, v. 52, no. 364, p. 1-26.
884 Şengör, A. M. C., 1984, The Cimmeride Orogenic System and the Tectonics of Eurasia, The Cimmeride Orogenic System
885 and the Tectonics of Eurasia, Volume 195, Geological Society of America, p. 0.
886 Smith, D. C., 1984, Coesite in clinopyroxene in the Caledonides and its implications for geodynamics: Nature, v. 310, no.
887 5979, p. 641-644.
888 Smith, J. V., 1974, Chemical and textural properties, Berlin Heidelberg New York, Springer, Feldspar minerals.
889 Sobolev, N. V., Dobretsov, N. L., Bakirov, A. B., and Shatsky, V. S., 1986, Eclogites from various types of metamorphic
890 complexes in the USSR and the problems of their origin: Geological Society of America Memoirs, p. 349-364.
891 Song, S., Niu, Y., Zhang, G., and Zhang, L., 2018a, Two epochs of eclogite metamorphism link 'cold' oceanic subduction
892 and 'hot' continental subduction, the North Qaidam UHP belt, NW China: Geological Society of London, v. 474,
893 p. 1-15.
894 Song, S. G., Bi, H. Z., Qi, S. S., Yang, L. M., Allen, M. B., Niu, Y. L., Su, L., and Li, W. F., 2018b, HP–UHP Metamorphic Belt
895 in the East Kunlun Orogen: Final Closure of the Proto-Tethys Ocean and Formation of the Pan-North-China
896 Continent: Journal of Petrology, v. 59, no. 11, p. 2043-2060.
897 Song, S. G., Niu, Y. L., Su, L., Zhang, C., and Zhang, L. F., 2014, Continental orogenesis from ocean subduction, continent
898 collision/subduction, to orogen collapse, and orogen recycling: The example of the North Qaidam UHPM belt,
899 NW China: Earth-Science Reviews, v. 129, p. 59-84.
900 Song, S. G., Su, L., Li, X. H., Niu, Y. L., and Zhang, L. f., 2012, Grenville-age orogenesis in the Qaidam-Qilian block: the
901 link between South China and Tarim: Precambrian Research, v. 220, p. 9-22.
902 Song, S. G., Zhang, l. F., Wei, C. J., Liou, J. G., and Sun, G. M., 2007, Eclogite and carpholite‐bearing metasedimentary

903 rocks in the North Qilian suture zone, NW China: implications for Early Palaeozoic cold oceanic subduction
904 and water transport into mantle Journal of Metamorphic Geology, v. 25, no. 5, p. 547-563.
905 Sun, J., Dong, Y., Ma, L., Chen, S., and Jiang, W., 2022, Devonian to Triassic tectonic evolution and basin transition in the
906 East Kunlun–Qaidam area, northern Tibetan Plateau: Constraints from stratigraphy and detrital zircon U–Pb
907 geochronology: GSA Bulletin, v. 134, no. 7-8, p. 1967-1993.
908 Sun, S. S., and McDonough, W. F., 1989, Chemical and isotopic systematic of Oceanic basalt: Implications for the
909 mantal composition and processes, Geological Society, London, Special Publications, 313-345 p.:
910 Syracuse, E. M., van Keken, P. E., and Abers, G. A., 2010, The global range of subduction zone thermal models: Physics
911 of the Earth and Planetary Interiors, v. 183, no. 1, p. 73-90.
912 Tang, H., Zhang, H. F., Zhang, M. J., Zou, H., and Zhang, J., 2022, Neoproterozoic and early Paleozoic metamorphism
913 recorded in gneisses from the East Kunlun Orogenic belt: Precambrian Research, v. 375.
914 Wang, B. Z., Luo, Z. H., Pan, T., Song, T. Z., Xiao, P. X., and Zhang, Z. Q., 2012, Petrotectonic assemblages and LA-ICP-MS
915 zircon U-Pb age of Early Paleozoic volcanic rocks in Qimantag area, Tibetan Plateau: Geological Bulletin of
916 China, v. 31, no. 6, p. 860-874.
917 Wang, G., Chen, N., Zhu, Y., and Zhang, K., 2003a, Late Caledonian Ductile Thrusting Deformation in the Central East
918 Kunlun Belt, Qinghai, China and Its Significance: Evidence from Geochronology: Acta Geologica Sinica - English
919 Edition, v. 77, no. 3, p. 311-319.
920 Wang, G., Chen, N., Zhu, Y., and Zhang, K., 2003b, Late Caledonian Ductile Thrusting Deformation in the Central East
921 Kunlun Belt, Qinghal, China and Its Significance: Evidence from Geochronology: Acta Geologica Sinica, v. 77,
922 no. 3, p. 311-319.
923 Wang, H., Wu, Y., Gao, S., Liu, X., Liu, Q., Qin, Z., Xie, S., Zhou, L., and Yang, S., 2013a, Continental origin of eclogites in
924 the North Qinling terrane and its tectonic implications: Precambrian Research, v. 230, no. Complete, p. 13-30.

925 Wang, H., Xiao, W., Windley, B. F., Zhang, Q. W. L., Tan, Z., Wu, C., and Shi, M., 2022a, Diverse P-T-t Paths Reveal High-
926 Grade Metamorphosed Forearc Complexes in NW China, v. 127, no. 6, p. e2022JB024309.
927 Wang, H. R., Zhao, H. G., Qiao, J. X., and Gao, S. H., 2013b, Theory and application of zircon U-Pb isotope dating
928 technique: Geology and Resources, v. 22, no. 3, p. 229-232.
929 Wang, H. Y. C., Chen, H.-X., Zhang, Q. W. L., Shi, M.-Y., Yan, Q.-R., Hou, Q.-L., Zhang, Q., Kusky, T., and Wu, C.-M., 2017,
930 Tectonic mélange records the Silurian–Devonian subduction-metamorphic process of the southern Dunhuang
931 terrane, southernmost Central Asian Orogenic Belt: Geology, v. 45, no. 5, p. 427-430.
932 Wang, J. M., Lanari, P., Wu, F. Y., Zhang, J. J., Khanal, G. P., and Yang, L., 2021, First evidence of eclogites overprinted by
933 ultrahigh temperature metamorphism in Everest East, Himalaya: Implications for collisional tectonics on early
934 Earth: Earth and Planetary Science Letters, v. 558.
935 Wang, Q., 2020, Geochemical Characteristics and Geological Significance of Eclogite in Airikehansen Area, Dulan
936 County, Qinghai Province: Northwestern Geology, v. 53, no. 1, p. 1-12.
937 Wang, Q., Zhao, J., Zhang, C., Yu, S., Ye, X., and Liu, X., 2022b, Paleozoic post-collisional magmatism and high-
938 temperature granulite-facies metamorphism coupling with lithospheric delamination of the East Kunlun
939 Orogenic Belt, NW China: Geoscience Frontiers, v. 13, no. 1, p. 101271.
940 White, R. W., Powell, R., Holland, T. J. B., Johnson, T. E., and Green, E. C. R., 2014, New mineral activity-composition
941 relations for thermodynamic calculations in metapelitic systems: Journal of Metamorphic Geology, v. 32, no. 3,
942 p. 261-286.
943 Whitney, D. L., and Evans, B. W., 2010, Abbreviations for names of rock-forming minerals: American Mineralogist, v. 95,
944 no. 1, p. 185-187.
945 Wood, B. J., 1973, Garnet-orthopyroxene and orthopyroxene-clinopyroxene relationship in simple and complex
946 systems: Contributions to Mineralogy&Petrology, v. 42, no. 2, p. 109-124.

947 Wu, C., Li, J., Zuza, A. V., Haproff, P. J., Chen, X., and Ding, L., 2021, Proterozoic− Phanerozoic tectonic evolution of the
948 Qilian Shan and Eastern Kunlun Range, northern Tibet: GSA Bulletin.
949 Wu, C., Liu, C., Fan, S., Zuza, A. V., Ding, L., Liu, W., Ye, B., Yang, S., and Zhou, Z., 2020, Structural analysis and tectonic
950 evolution of the western domain of the Eastern Kunlun Range, northwest Tibet: GSA Bulletin, v. 132, no. 5-6,
951 p. 1291-1315.
952 Wu, C., Zuza, A. V., Chen, X., Ding, L., Levy, D. A., Liu, C., Liu, W., Jiang, T., and Stockli, D. F., 2019, Tectonics of the
953 Eastern Kunlun Range: Cenozoic reactivation of a Paleozoic - early Mesozoic orogen: Tectonics, v. 38, no. 5, p.
954 1609-1650.
955 Wu, Y., and Zheng, Y., 2004, Genesis of zircon and its constraints on interpretation of U-Pb age: Chinese Science
956 Bulletin, v. 49, no. 15, p. 1554-1569.
957 Wu, Y. B., and Zhen, Y. F., 2004, Study on mineralogy of zircon formation and its constraints on U-Pb age interpretation:
958 Chinese Science Bulletin, v. 49, no. 16, p. 1589-1604.
959 Xia, B., Cui, Y., Shang, Y. F., and Shi, J. T., 2022a, Petrology of Eclogite at Huwan, Western Dabie and Implications for
960 Phase Equilibrium Modeling on LT-HP/UHP Eclogite: Journal of Earth Science. doi.org/10.1007/s12583-022-
961 1719-9.
962 Xia, B., Shang, Y. F., Lu, X. B., and Wu, Y. B., 2022b, UHP eclogite from western Dabie records evidence of polycyclic
963 burial during continental subduction: American Minerologist. doi.org/10.2138/am-2022-8446
964 Xiao, W. J., Windley, B. F., Yong, Y., Yan, Z., Yuan, C., Liu, C. Z., and Li, J. L., 2009, Early Paleozoic to Devonian multiple-
965 accretionary model for the Qilian Shan, NW China: Journal of Asian Earth Sciences, v. 35, no. 3-4, p. 323-333.
966 Xu, X., Song, S., and Su, L., 2016, Formation age and tectonic significance of the Wanbaogou basalts in the middle East
967 Kunlun orogenic belt: ACTA PETROLAGICA ET MINERALOGICA, v. 35, no. 6, p. 16.
968 Yang, J. S., Jiang, C. F., Feng, B. G., Zhu, Z. Z., Zhao, M., Shi, X. D., and Hu, J. Q., 1986, An outline on the tectonics of the

969 Kunlun region: Bulletin of the Institute of Geology Chinese Academy of Geological Sciences, v. 2, p. 010.
970 Yang, J. S., Robinson, P. T., Jiang, C. F., and Xu, Z. Q., 1996, Ophiolites of the Kunlun Mountains, China and their tectonic
971 implication: Tectonophysics, v. 258, no. 1-4, p. 215-231.
972 Yang, J. S., Wang, X. B., Shi, R. D., Xu, Z. Q., and Wu, C. L., 2004, The Dur'ngoi ophiolite in East Kunlun, northern
973 Qinghai-Tibet Plateau: a fragment of paleoTethyan oceanic crust: Zhongguo Dizhi(Geology in China), v. 31, no.
974 3, p. 225-239.
975 Yu, J., Zheng, Y., Xu, R., Hou, W., and Cai, P., 2020a, Zircon U-Pb Chronology, Geochemistry of Jiangjunmu Ore-Bearing
976 Pluton, Eastern Part of East Kunlun and Their Geological Significance: Earth Science, v. 45, no. 4, p. 1151-1167.
977 Yu, M., Dick, J. M., Feng, C., Li, B., and Wang, H., 2020b, The tectonic evolution of the East Kunlun Orogen, northern
978 Tibetan Plateau: A critical review with an integrated geodynamic model: Journal of Asian Earth Sciences, v.
979 191, p. 104168.
980 Yu, S., Zhang, J., Li, H., Hou, K., Mattinson, C. G., and Gong, J., 2013a, Geochemistry, zircon U-Pb geochronology and Lu-
981 Hf isotopic composition of eclogites and their host gneisses in the Dulan area, North Qaidam UHP terrane:
982 New evidence for deep continental subduction: Gondwana Research, v. 23, no. 3, p. 901-919.
983 Yu, S., Zhang, J. X., Gong, J. H., and Li, Y. S., 2013b, Research on HP granulite-facies metamorphism and anatexis: A case
984 study of Dulan area in the North Qaidam Mountains: Acta Petrologica Sinica, v. 29, no. 6, p. 2061-2072.
985 Zhang, G. B., Ellis, D. J., Christy, A. G., Zhang, L. F., and Song, S. G., 2010a, Zr-in-rutile thermometry in HP/UHP eclogites
986 from Western China: Contributions to Mineralogy&Petrology, v. 160, no. 3, p. 427-439.
987 Zhang, G. B., Ireland, T., Zhang, L. F., Gao, Z., and Song, S. G., 2016, Zircon geochemistry of two contrasting types of
988 eclogite: Implications for the tectonic evolution of the North Qaidam UHPM belt, northern Tibet: Gondwana
989 Research, v. 35, p. 27-39.
990 Zhang, G. B., Niu, Y. L., Song, S. G., Zhang, L. F., Tian, Z. L., Christy, A., and Han, L., 2015a, Trace element behavior and P-

T-t evolution for partial melting of exhumed eclogite in the North Qaidam UHPM belt (NW China): implications for adakite genesis: Lithos, v. 226, p. 65–80.

Zhang, G. B., Zhang, L. F., and Song, S. G., 2012, An overview of the tectonic evolution of North Qaidam UHPM belt: From oceanic subduction to continental collision: Geological Journal of China Universities, v. 18, no. 1, p. 28-40.

Zhang, J. X., Mattinson, C. G., Meng, F. C., Wan, Y., and Tung, K., 2008, Polyphase tectonothermal history recorded in granulitized gneisses from the north Qaidam HP/UHP metamorphic terrane, western China: Evidence from zircon U-Pb geochronology: Geological Society of America Bulletin, v. 120, no. 5-6, p. 732-749.

Zhang, J. X., Meng, F. C., Li, J. P., and Mattinson, C. G., 2009, Coesite in eclogite from the North Qaidam Mountains and its implications: Chinese Science Bulletin, no. 6, p. 1105-1110.

Zhang, J. X., Meng, F. C., Wan, Y. S., Yang, J. S., and Dong, G. A., 2003, Early Paleozoic tectono-thermal event of the Jinshuikou Group on the southern margin of Qaidam:Zircon U-Pb SHRIMP age evidence: GEOLOGICAL BULLETIN OF CHINA, v. 22, no. 6, p. 397-404.

Zhang, J. X., Yu, S. Y., Li, Y. S., Yu, X. X., Lin, Y. H., and Mao, X. H., 2015b, Subduction, accretion and closure of Proto-Tethyan Ocean: Early Paleozoic accretion/collision orogeny in the Altun-Qilian-North Qaidam orogenic system: Acta Petrologica Sinica, v. 31, no. 12, p. 3531-3554.

Zhang, J. X., Yu, S. Y., and Mattinson, C. G., 2017, Early Paleozoic polyphase metamorphism in northern Tibet, China: Gondwana Research, v. 41, p. 267-289.

Zhang, Y. F., Pei, X. Z., Ding, S. P., Li, R. B., Feng, J. Y., Sun, Y., Li, C., and Chen, Y. X., 2010b, LA-ICP-MS zircon U-Pb age of quartz diorite at the Kekesha area of Dulan County, eastern section of the East Kunlun orogenic belt, China and its significance: Geological Bulletin of China, v. 29 no. 1, p. 79-85.

Zhang, Y. L., Zhang, X. J., Hu, D. G., Shi, Y. R., and Lu, L., 2010c, SHRIMP zircon U-Pb ages of rhyolite from the Naij Tal

group in the East Kunlun orogenic belt: Journal of Geomechanics, v. 16, no. 1, p. 21-27.

Zhao, G. C., Wang, Y. J., Huang, B. C., Dong, Y. P., Li, S. Z., Zhang, G. W., and Yu, S., 2018, Geological reconstructions of the East Asian blocks: From the breakup of Rodinia to the assembly of Pangea: Earth-Science Reviews, v. 186, p. 262-286.

Zheng, Y.-F., Zhang, L., McClelland, W. C., and Cuthbert, S., 2012, Processes in continental collision zones: Preface: Lithos, v. 136-139, p. 1-9.

Zhou, W., Xiaocheng, z., and Xinbiao, L., 2020, Petrology, Geochemistry and Chronology of the Baishahe Formation in Numohong Area of Eastern Kunlun Orogenic Belt: Journal of Earth Science, v. 45, no. 12, p. 4370-4388.

Zuza, A. V., Wu, C., Reith, R. C., Yin, A., Li, J., Zhang, J., Zhang, Y., Wu, L., and Liu, W., 2017, Tectonic evolution of the Qilian Shan: An early Paleozoic orogen reactivated in the Cenozoic: GSA Bulletin, v. 130, no. 5-6, p. 881-925.

Figure and Table captions

Figure captions:

Figure 1. (A) The location of the northern part of Qinghai-Tibet Plateau. (B) Geological sketch map of the East Kunlun Orogenic belt (modified after (Meng et al., 2017; Zhang et al., 2015b; Zhang et al., 2017)) and the location of the eclogites in the Nuomuhong area and other segments (Meng et al., 2013b; Qi et al., 2014; Qi et al., 2016a; Song et al., 2018b). (C) The approximately N-S structural cross-section of the Nuomuhong area showing main rock types and the location of samples.

Figure 2. Field photographs of eclogite at Nuomuhong, in East Kunlun. (A) Eclogite block enclosed in the host felsic gneiss. (B) Eclogite retrograded to amphibolite at edges. The red dashed line marks the boundary between the retrograde eclogite and amphibolite. (C) The red dashed line showing boundary between retrograde eclogite and the host felsic gneiss. (D) Marble intercalated in amphibolite that showing banded structure. (E) The host felsic gneiss consisted mainly of felsic minerals, biotite and garnet. (F) The retrograde eclogite consisted of mainly garnet, clinopyroxene, amphibole and quartz.

Figure 3. Photomicrographs of representative eclogite at Nuomuhong, EKOB. Mineral abbreviations are after Whitney and Evans (2010). (A) A large garnet porphyroblast from the eclogite LH 3–5 showing apparent zoning with abundant inclusions in the reddish core and minor in the light rim. Amphibole (Amp II), plagioclase, ilmenite and biotite (Bt) develop around the garnet. (B) Backscattered electron image (BSE) of the garnet porphyroblast in Fig.

3A showing inclusions of titanite (Ttn) and omphacite (Cpx I_a) in the core. (C–D) Corona of plagioclase (Pl III) + amphibole (Amp II) ± ilmenite (LH3–4) around a relict garnet porphyroblast with inclusions of omphacite (Cpx I_a). Symplectite of plagioclase (III) + amphibole develops in the matrix; (E–F) Symplectite of orthopyroxene (Opx)+ plagioclase (Pl II) around relict omphacite in matrix from the sample LH3–4. Corona of symplectite amp II + Pl develops around relict garnet and low-sodic clinopyroxene (Cpx II_a; light-colored in BSE) develops around relict omphacite porphyroblast (Cpx I_b; dark-colored in BSE). (G) Locally enlarged BSE image in Fig. 3D showing transition from relict omphacite porphyroblast (Cpx I_b; with no Opx) to clinopyroxene porphyroblast (Cpx II_b; with Opx), then to symplectite of Amp II + Pl II; (with Opx). Corona of plagioclase (Pl III) + amphibole (Amp II) rims garnet; (H) Rutile as inclusions in garnet or in matrix from the sample LH 3–2. It has been partial replaced by ilmenite; (I) Amphibole (Amp I) included in garnet from sample LH 3–2. (G–K) Plane-polarized photo with corresponding BSE image showing Biotite around amphibole (Amp II) from sample LH 3–5.

Figure 4. Backscattered electron image of the garnet porphyroblast (LH 3–4) with EPMA composition section (A, B) and the locally enlarged photo of inclusions (3) with the mineral assemblage of Ep + Pl (Ab). (D) Diagram showing the compositional variation of garnet porphyroblast, the $Grt_{(mantle+core)}$ (Grt I) and Grt_{rim} (Grt II) are both group C-type after Coleman et al. (1965). (E) Zoning profile of X_{alm} [=Fe^{2+}/(Fe^{2+} + Mn + Mg + Ca), X_{sps} , X_{prp} and X_{grs} defined accordingly across garnet in the eclogite samples LH 3–4 from the Nuomuhong area].

Figure 5. Mineral chemistry diagrams. (A–B) Ternary classification diagrams for pyroxenes of the Nuomuhong eclogites, after Morimoto (1988): (A) The classification diagram for Quad-Jd-Ae. (B) The classification diagram for Wo-En-Fs. (C–D) The classification diagrams for amphiboles of Nuomuhong eclogite, after Leake et al. (2004) and Song et al. (2018b). (E) Ab–An–Or diagram showing the composition of plagioclase, after Smith (1974); Ab=X_{Na}=Na/(Ca + K + Na); An=X_{Ca}=Ca/(Ca + K + Na); Or =X_K=K/(Ca + K + Na).

Figure 6. Mineral assemblages for different metamorphic stages. Solid lines indicate minerals present in the samples, whereas the dashed line refers to inferred minerals.

Figure 7. Raman spectra of (A) omphacite (Omp) inclusions, (B) omphacite/jadeite inclusions, and (C) garnet (Grt) and omphacite inclusions in zircon (Zrn) grains from the Nuomuhong retrograde eclogite, middle East Kunlun orogen.

Figure 8. Chondrite-normalized REE distribution patterns (A) and primitive mantle-normalized spidergram of the retrograde eclogites and garnet amphibolites (B). The chondrite and primitive mantle values are from (Sun and McDonough, 1989).

Figure 9. (A–B) Zircon CL images, (C) SHRIMP U–Pb age concordia diagram and weighted mean $^{206}Pb/^{238}U$ ages and (D) Chondrite-normalized REE distribution patterns for the Nuomuhong retrograde eclogite LH3–4.

Figure 10. (A) *P–T* pseudosection for Nuomuhong eclogite sample LH 3–4 (MnNCKFMASHTO system); (B) Grossular [Ca/(Ca+Mg+Fe+Mn) *100] and pyrope [Mg/(Ca+Mg+Fe+Mn) *100] isopleths.

Figure 11. Tectonic discrimination diagrams (A–D) for the retrograde eclogite (A) Zr–Zr/Y diagram (Pearce and Norry, 1979); (B) Ce/Yb–Ta/Yb diagram (Pearce, 1982); (C) Y–La–Nb diagram (Cabanis and Lecolle, 1989); (D) Nb–Zr–Y diagram (Meschede, 1986); (E) AFM diagram (Irvine and Baragar, 1971). WPB–Within Plate Basalts; IAB–Island Arc Basalts; MORB–Mid-Ocean Ridge Basalts.

Figure 12. The *P–T* path for the Nuomuhong eclogite in this study, in comparision with eclogite in the eastern segment of the East Kunlun orogen from Song et al. (2018b). Boundaries for varies metamorphic facies, High-P granulite, UHT follow Schreyer (1988), Syracuse et al. (2010) and Maruyama et al. (1996), metamorphic facies, their abbreviations, and phase equilibria are after Liou et al. (2004).

Figure 13. Tectonic model for the Eastern Kunlun orogen, and Proto-Tethys Ocean.

Table captions:

Table S1. Representative electron microprobe analyses of garnet in eclogite samples.

Table S2. Representative analyses of clinopyroxene (omphacite)in eclogite samples.

Table S3. Representative microprobe analyses of low-sodic clinopyroxene in eclogite samples.

Table S4. Representative microprobe analyses of amphibole in eclogite samples.

Table S5. Representative microprobe analyses of plagioclase in eclogite samples.

Table S6. Representative microprobe analyses of other minerals (orthopyroxene and epidote) in eclogite samples

Table S7. Whole rock major (wt%) and trace element (ppm) analyses of eclogites in Nuomuhong area, EKOB.

Table S8. SHRIMP Zircon U-Pb isotopic data from the eclogite in Nuomuhong area, EKOB.